MITIGATION OF ICE-INDUCED VIBRATIONS OF OFFSHORE WIND TURBINES BY CONTROL IDLING

Irfan Ali

TU Delft

MITIGATION OF ICE-INDUCED VIBRATIONS OF OFFSHORE WIND TURBINES BY CONTROL IDLING

MASTER OF SCIENCE THESIS

For obtaining the degree of Master of Science in
Offshore and Dredging Engineering at Technische Universiteit Delft

Faculty of Civil Engineering, Mechanical Engineering and Marine Technology,
28 August, 2019

Committee:	Prof. Dr. A. Metrikine	TU Delft - Chairman
	Dr. Ir. H. Hendrikse	TU Delft - Asst. Prof.
	Dr. F. Pisanò	TU Delft - Asst. Prof.
	Ir. C. C. Owen	TU Delft - PhD Student

TU Delft Delft University of Technology

For a successful technology, reality must take precedence over public relations, for nature cannot be fooled.

Richard P. Feynman

PREFACE

This master thesis is submitted as part of the requirement for obtaining the degree of Master of Science in Offshore and Dredging Engineering at the Delft University of Technology (TU Delft) in the Faculty of Civil Engineering and Geosciences. I would like to express my sincere gratitude to everyone for their support and guidance throughout this work.

First and foremost, I would like to start by thanking Hayo Hendrikse for opening an exciting new world of ice-structure interaction to me. I completely enjoyed working on the topic throughout the nine months. Among other things, I appreciate a lot that he replied to all my emails promptly given his busy schedule. I would also like to thank Cody Owen for being available on short notices. It was always helpful to bat ideas about my research around with you. Furthermore, I want to extend my thanks to Andrei Metrikine for his continued advice towards the constant improvement of my work. And finally, I warmly thank Pim van der Male and Carlos J. Simao Ferreira for their initial guidance on the aerodynamics of the wind turbine.

Words fail to express my appreciation to my parents, and my wife, Nazia, for their persistence support throughout my study. Amongst many, I want to thank my sister, Abida, for designing the title page. Just as importantly, I am grateful to all of my friends in TU Delft for their unwavering support during this 2-year master program.

I hope you enjoy your reading.

Irfan Ali
Delft, August 2019

SUMMARY

Offshore wind farms are being developed at locations with moderate ice conditions such as the Baltic Sea, where drifting sea ice upon interacting with offshore structures could lead to the development of a phenomenon known as Ice-induced vibrations, the most severe of which can significantly contribute to the fatigue damage of the structure. These vibrations are especially severe when the turbine is idling. Current mitigation measures consist of an expensive solution of ice cones, which are only favourable when ice occurs seasonally. The main objective of this study is to investigate numerically a novel approach to mitigate the ice-induced vibrations of offshore wind turbines by means of control idling.

Three regimes of ice-induced vibrations are generally distinguished, viz. intermittent crushing (ICR), frequency lock-in (FLI), and continuous brittle crushing (CBR). Among these regimes, the ICR and FLI can cause significant vibrations in the offshore structure. Preceding the ice action, the investigation of rotor aerodynamics during the parked condition shows that for wind speeds below the cut-in wind speed of the rotor, the turbine operates in the unsteady aerodynamics termed as dynamic inflow. To include this unsteadiness into the aerodynamic model, the "Stig Øye Dynamic Inflow" engineering model is implemented into the steady Blade Element Momentum method. To that end, a finite difference structural model for a 5-MW reference offshore wind turbine is developed that enables the coupling between the structure, rotor aerodynamics, and ice.

In this study, the comparative analyses are made between the two cases: one with the ice action only, and, the other with the combined effect of ice and wind, where the rotational rotor speeds chosen are 3.0rpm, 6.9rpm and 12.1rpm. In the ice-action case, it is found that the structural response frequency during the ICR and FLI is around the first and the second natural frequency of the structure, respectively. In the case of ice and wind, it is found that the unsteady BEM method has certain limitations, especially in the intermittent crushing regime. Also, the aerodynamic damping has no notable effect on the range of ice-induced vibration regimes for the rotor speed of 6.9rpm and 12.1rpm. However, it does have a significant effect for the rotor speed of 3.0rpm. The quantitative comparison of fatigue damage between the two cases showcases that for the majority of ice-sheet velocities during ICR and FLI, the damage is found to be greater in the ice and wind case. Based on the results, it is concluded that the rotor aerodynamics does help in damping the vibrations in the ICR regime, but in the FLI regime, it has no significant impact when specific ice-drift speeds are considered. It can also be confirmed that by the careful selection of the rotational rotor speed, the range of ice-induced vibration regime can be influenced. However, to draw the general conclusion, the analysis needs to be conducted for varied ranges of rotor speeds. Also, the present framework of the aerodynamic model needs to be improved to capture the vortex-ring flow state to predict the rotor aerodynamics accurately for all the ice-sheet velocities.

CONTENTS

1

INTRODUCTION

Offshore wind energy has been the most stable source of renewable energy in Europe, where the ongoing developments are aimed to make the energy more attractive and cost-effective in order to compete with fossil fuel energy resources. With the advancement in the offshore wind industry and to meet the targets set by the European Wind Energy Association (Arapogianni et al., 2013), the offshore wind farms are being developed at locations with moderate ice conditions such as the Baltic Sea, where the wind conditions are favourable.

Most offshore wind turbines are supported by relatively cheap monopile foundations with diameters ranging from 6m at the waterline to more than 8m within the seabed (Seidel and Hendrikse, 2018). Due to the uncertainties in the environmental loading, these structures are generally designed with the conservative approach, resulting in overdesign of the support structure. Therefore, it is vital for the sustained development of the offshore wind industry in the ice-infested waters that the offshore structures are designed to be safe and cost-effective.

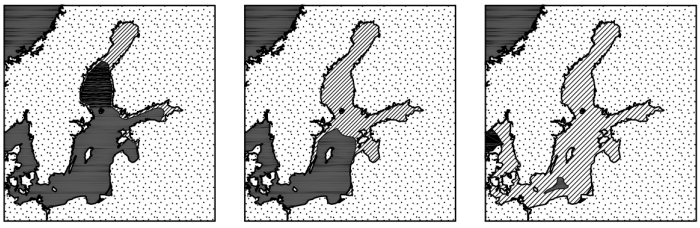

Figure 1.1: Baltic Sea ice cover (ISO 19906, 2010). Dashed line indicates the ice coverage during different winter conditions.

Offshore structures in cold regions are needed to be designed to withstand loading from sea ice. In temperate regions, such as the Baltic Sea or large lakes, that mainly

concerns the loads from ice ridges and level ice. Figure 1.1 shows a map of ice cover in the Baltic Sea during mild, moderate, and severe winter.

Ridges are of primary concern for impact and static loading, whereas level ice upon interacting with a vertically sided offshore structure can lead to the development of structural vibrations commonly referred to as ice-induced vibrations. In the early stages of Bohai Sea oil exploitation, two multi-leg jacket platforms were pushed-over upon interacting with the sea ice. Furthermore, other jackets that were designed too conservatively were found with severe problems of strong vibrations that resulted in accidents during the drilling operations (Yue and Li, 2003). Also, in the past, the ice-induced vibrations have resulted in the failure of structural members of lighthouses in the Gulf of Bothnia (Bjork, 1981). In 1986, in the Canadian Beaufort Sea, severe vibrations were observed in the Molikpaq caisson facility that jeopardized the platform's stability (Jefferies and Wright, 1988). Since the design standards were not mature enough during the early stages of offshore development, these problems were frequent in ice infested waters.

Ice-induced vibrations originate when the ice interacts with the structure in dynamic manner resulting in high global peak loads, and thereby, significantly contribute to the fatigue of structures. With the development of the offshore wind industry, specific questions concerning the interaction between level ice and relatively slender, flexible structures have gained renewed interest (Barker et al., 2005). Solutions to mitigate the risks of interaction between the ice and offshore wind turbine, primarily fixed ice breaking cones (Brown and Määttänen, 2009), have already been applied and were effective in reducing the ice force. However, these conical structures are expensive, and the increased diameter at the mean sea level results in higher wave loading for the more significant part of the year. Therefore, an alternative method is required that can influence the ice-structure interaction process.

1.1. RESEARCH MOTIVATION

Offshore wind turbine foundations are designed for level ice loading in extreme and fatigue conditions, according to IEC-61400 (2017). The application of the industry standard methods assumes that the ice load is unaffected by the structural motions. On the contrary, based on the extensive research on ice-induced vibrations, it is known that the load exerted by ice depends on the structural response.

Alternatively, several phenomenological models exist for predicting the dynamic ice-structure interaction. In this study, the phenomenological ice model proposed and validated by Hendrikse et al. (2019) is implemented and coupled with an offshore wind turbine monopile-type support structure. The proposed phenomenological model is based on the theory, presented in Hendrikse (2017), that the ice-structure interaction are governed by the contact area variation, and the rate-dependent deformation and failure behaviour of the ice.

ISO 19906 (2010) typically distinguishes three interaction regimes, wherein the regimes of intermittent crushing and frequency lock-in are the most critical for the design of offshore wind support structure. The large load drops that occur during intermittent crushing may be critical for the rotor-nacelle-assembly, whereas the sustained high amplitude oscillation during frequency lock-in may significantly contribute to the fatigue of structure.

Effects are considered to be most significant during turbine idling (or parked condition) as the reduced aerodynamic damping is known to have a significant effect on the development of ice-induced vibrations. To the author's knowledge, full-scale observations of ice-induced vibrations of offshore wind turbines are not yet available in the public domain, although the model-scale test results have been presented by Barker et al. (2005). Often, the ice loads will not be the design driving. However, a significant reduction in their impact may be economically beneficial where the expected occurrence of ice is more. In the current study, the author aspires to mitigate these vibrations by employing the application of wind turbine's control idling that may provide an alternative to the expensive solution of ice cones.

1.1.1. CURRENT PRACTICES ON MITIGATING ICE-INDUCED VIBRATIONS

Several mitigation measures have been proposed to avoid ice-induced vibrations of the offshore platform. Reiterating, ice-breaking cones are the most common approach and have been implemented on several platforms. The sloping cones make the ice to move up or down and change the failure mode from crushing to bending, thereby reducing the possibility of ice-induced vibrations (Brown and Määttänen, 2009). Several researchers have demonstrated the effectiveness of conical waterline geometry in reducing the ice force (Frederking and Schwarz (1982), Wessels and Kato (1988), Shkhinek et al. (1996), Barker et al. (2005), Gravesen et al. (2005)). However, based on the full-scale test carried out in the Bohai Sea, Yue and Bi (2000) found that the large structural vibrations still exists when the breaking (or bending) frequency falls close to the natural frequency of the structure.

Kärnä (1994), on the other hand, conducted numerical studies and concluded that the steady-state vibrations generated from the ice-structure interaction can be prevented by providing a sufficient amount of damping. Kärnä and Kolari (2004) demonstrated the effectiveness of passive devices, such as Tuned Mass Dampers (TMD) to mitigate the vibrations in offshore wind turbines. Furthermore, Zhang et al. (2008) and Yue et al. (2009) conducted experimental studies on jacket platforms in the JZ20-2 oil field to investigate the effectiveness of TMD and demonstrated that the passive device could favourably reduce the dynamic response of the platform. However, the major drawback associated with the TMD in an offshore wind turbine is the large mass at tower top, which is undesirable due to the installation issues. Mróz et al. (2008) proposed a semi-active solution of *smart cone* that utilizes the compliant connection between the cone and tower instead of fixed connection. The idea is to decrease the horizontal component of ice loading at the conical surface, which causes the tower vibration. Numerical studies were carried out to demonstrate the effectiveness of the new solution. Wang et al. (2013) proposed an isolation cone system to mitigate the ice-induced vibrations and demonstrated its effectiveness by conducting numerical simulations on JZ20-2MUQ jacket platform.

1.2. RESEARCH OBJECTIVES AND SCOPE

The current measures used to mitigate ice-induced vibrations for the offshore structures are either expensive or are undesirable due to the installation problems. Therefore, the aim of this thesis is:

1

To investigate numerically a novel approach to mitigate the ice-induced vibrations of offshore wind turbines by means of control idling.

Control idling in this study is referred to as the aerodynamics of wind turbine rotating at constant rotational speed during the parked condition.

In the following sub-section, I briefly layout the sub-research objectives in order to address the specific research questions.

1.2.1. RESEARCH QUESTIONS

The main aim of the thesis is first addressed by asking the following research questions:

1. What percentage of aerodynamic damping can be introduced into the structure below the cut-in wind speed of the rotor by means of control idling?
2. How does the control idling help in reducing the possibility of intermittent crushing and frequency lock-in?

1.2.2. RESEARCH OBJECTIVES

These research questions define the scope of the study and set the following sub-research objectives:

1. To create a coupled model for non-linear dynamic ice-structure interaction of offshore wind turbine structures;
2. To introduce an aerodynamic model that can capture rotor aerodynamics of a wind turbine operating below cut-in wind speed at a constant rotational speed and subsequently, enable coupling with the dynamic ice-structure interaction;
3. To investigate the effectiveness of rotor aerodynamics in mitigating the ice-induced vibrations over the range of ice-sheet velocities:
   (a) To compare the range of intermittent crushing and frequency lock-in for different rotational rotor speeds;
   (b) To study the effect of rotor aerodynamics in mitigating these vibrations;
   (c) To present the results in terms of fatigue damage to show the potential effect of the rotor aerodynamics on structural vibrations.

1.3. THESIS OUTLINE

This thesis is organized in the following way. First, in Chapter 2, the details of the ice-structure interaction with the flexible, vertically sided offshore structures are presented. At the end of this chapter, the phenomenological ice model developed by Hendrikse et al. (2019) used in the current study is given. Chapter 3 deals with the aerodynamics of the wind turbine operating below the cut-in wind speed of the rotor based on the Blade Element Momentum method. Then, in Chapter 4, the couple aero-ice-structure model of the offshore wind turbine is numerically implemented and described in detail. In Chapter 5, the results obtained from the numerical model for varying ice-sheet velocities and rotational rotor speeds are analyzed and shown. Finally, the main findings of this thesis and recommendations for further research are summarized in Chapter 6.

2

ICE-STRUCTURE INTERACTION

Level ice upon interacting with the vertically sided offshore structures can fail in various manner, depending on the indentation velocity of ice, ice thickness and the structural properties. In this chapter, the interaction of level ice against a flexible, vertically sided structure is introduced. First, in Section 2.1, the dynamic interaction between the ice and structure, which can lead to the development of ice-induced vibrations is briefly discussed. Finally, in Section 2.2, an overview of phenomenological ice model developed by Hendrikse et al. (2019) is given along with the ice input parameters adopted in the current study. For detailed information on the ice-induced vibrations and the ice model, the reader is advised to refer to Hendrikse (2017).

2.1. ICE-INDUCED VIBRATIONS

A flexible (or compliant) structure interacts with ice in a dynamic manner. During the dynamic ice-structure interaction, the structure starts vibrating in its fundamental mode of vibrations; this phenomenon is known as *Ice-induced vibrations*. The ice-induced vibrations are associated with the crushing failure mode of ice and therefore corresponds to the cases of low aspect ratio or relatively thick ice (Hendrikse, 2017).

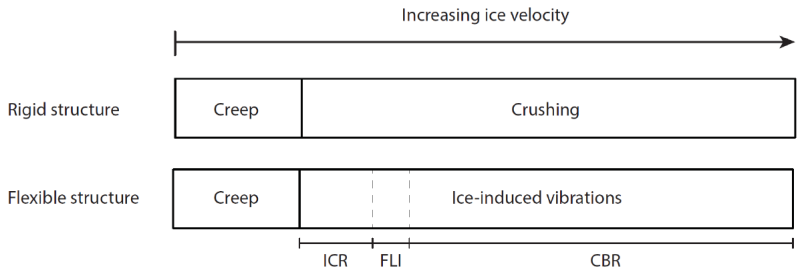

Figure 2.1: Schematic representation of ice-structure interaction on rigid and flexible vertically sided offshore structure with increasing ice velocity (Hendrikse, 2017). Note that the ICR and FLI do not always develop.

Within the crushing failure mode, three regimes of ice-induced vibrations are distinguished by ISO 19906 (2010), which are defined as intermittent crushing, frequency lock-in, and continuous brittle crushing. In the order of increasing ice sheet velocities as illustrated in Figure 2.1, intermittent crushing is typically observed at low indentation velocities, followed by frequency lock-in, and in the end at higher velocities continuous brittle crushing is observed.

Among these regimes, intermittent crushing and frequency lock-in are of particular interest, as the former is associated with the largest global ice-induced loads, whereas the latter has significant structural oscillations. Typical time dependence of global ice-induced loads and structural displacement at ice action point in each of these regimes is shown in Figure 2.2.

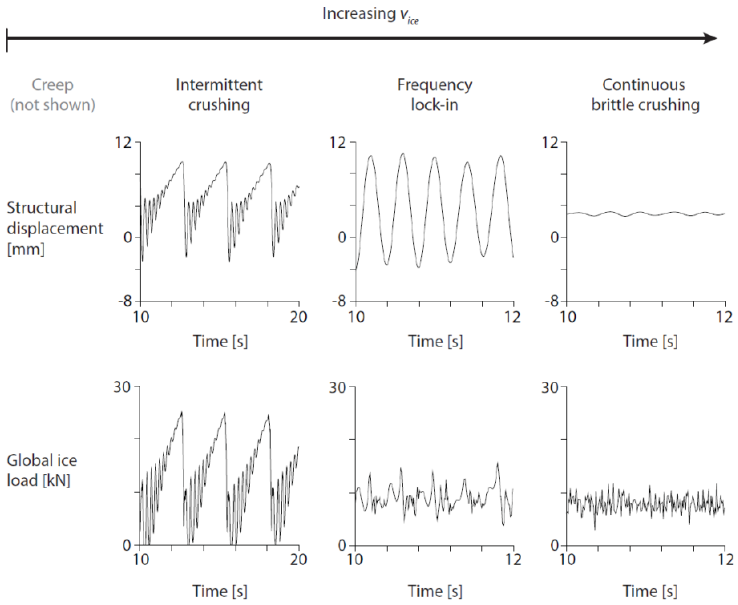

Figure 2.2: Illustration of typical time signals of structural displacement and global ice load in the ice-induced vibration regimes (Hendrikse, 2017). The values shown were obtained from numerical simulations and does not reflect real measurements.

2.1.1. INTERMITTENT CRUSHING

Intermittent crushing occurs when a flexible structure with low stiffness interacts with a slowly moving ice sheet (Hendrikse, 2017)). This regime is characterized by the saw-tooth pattern of global ice load and structural displacement as depicted in the Figure 2.2. It has been observed that the saw-tooth frequency remains approximately constant and increases with increasing ice velocity until the other two ice-induced vibrations become dominant. The maximum global ice load in this regime is significantly higher as compared to frequency lock-in and continuous brittle crushing. Furthermore, based on the experimental observation made by Hendrikse (2017), the relative velocity between ice and structure plays a significant role during intermittent crushing.

2.1.2. FREQUENCY LOCK-IN

Frequency lock-in can be invoked over a range of ice drift velocities for structures with low damping and low natural frequencies (Hendrikse, 2017). In frequency lock-in, the structure undergoes harmonic oscillations at a frequency slightly smaller than one of its natural frequencies as portrayed in Figure 2.2.

FREQUENCY LOCK-IN RELATION

During frequency lock-in, a nearly linear relation exists between the maximum structural velocity and ice sheet velocity, as depicted in Figure 2.3. The relation between the velocities at ice action point is given in Equation 2.1 and can be used as a guidance to distinguish the frequency lock-in from other types of harmonic oscillations of the structure.

$$\dot{u}_{max} = \beta v_{ice} \tag{2.1}$$

where $\dot{u}_{max}$ is the maximum structural velocity at ice action point, v_{ice} is the ice sheet velocity and the value of β varies between 1.0 and 1.5 but not exclusively limited to this range.

Damping has a significant effect on the boundaries of the range of velocities for which frequency lock-in can develop and is of particular interest in this study. The range of ice-sheet velocities is observed to be sufficiently broad when the damping is assumed to be small. Furthermore, a critical observation made by Hendrikse (2017) on a single-degree-of-freedom system is that the higher damping in the structure reduces the range of velocities over which the frequency lock-in can develop, where the effect is more pronounced on the upper boundary of ice-drift speed than the lower one.

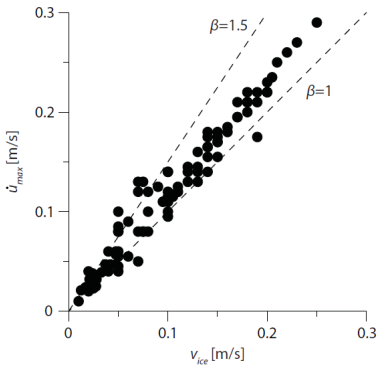

Figure 2.3: Maximum velocity of structural oscillations versus ice sheet velocity during frequency lock-in replotted by Hendrikse (2017).

2.1.3. CONTINUOUS BRITTLE CRUSHING

Continuous brittle crushing occurs in all flexible structures at high ice-sheet velocities. In this regime, the relative velocity between the ice and structure remains high, and therefore, ice deforms in a brittle manner. Figure 2.2 shows that the ice load signal is random in nature and oscillates around a constant mean value. Furthermore, the structural

response is similar to that of a structure being excited by an aperiodic load. Overall, the amplitude of structural oscillations and the maximum global ice load are significantly smaller as compared to the frequency lock-in and intermittent crushing, indicating that the ice-structure interaction within this regime is insignificant.

2.2. ICE MODEL

In literature, several phenomenological models and theories exist that explains the occurrence of ice-induced vibrations based on the two main schools of thought. The first attributes ice-induced vibrations as a result of negative damping; decrease in global load with increasing ice velocity. Alternatively, the second common approach is to define a characteristic failure length of the ice, where the ice fails with distinct fracture frequency, often called spalling frequency. This fracture frequency is usually close to one of the natural frequencies of the structure, thereby resulting in resonance between ice and structure. Hendrikse (2017) concluded that neither of these approaches provides a complete and consistent theory for level ice interacting with vertically-sided offshore structures.

The phenomenological model developed by Hendrikse (2017) (and later modified by Hendrikse et al. (2019)) is based on the mechanism that the variations in the contact area between ice and structure govern the global ice loads, and therefore, is the source of ice-induced vibrations. The applicability of the numerical model is verified against the key observations from the literature and the experimental cases presented in Hendrikse and Metrikine (2015).

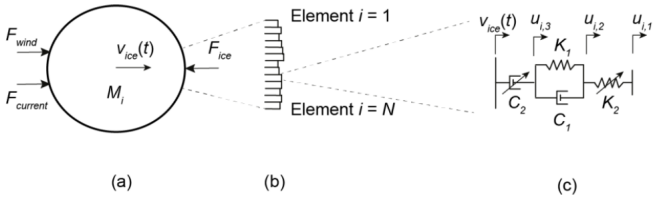

Figure 2.4: (a) Drifting ice floe interacting with cylindrical structure (b) Ice edge partitioned into N independent elements with an individual offset to the structure (c) Each ice element modelled as combination of springs and dashpots to capture elastic, delayed-elastic and viscous deformation (Hendrikse et al., 2019).

2.2.1. MODEL DESCRIPTION

The basic principle behind the proposed model is that a larger contact area develops between the ice and structure when ice is moving slowly in contrast to the smaller contact area when the ice is loaded quickly. The ice sheet is partitioned into N independent ice elements along the ice-structure interface, denoted by i, as illustrated in Figure 2.4, to reproduce the stochastic effect of contact area variation within the model. Each element consists of combinations of springs and dashpots that represents the visco-elastic behaviour of ice. The spring and dashpots in each element allow modelling elastic and inelastic deformation, and local failure of ice. A short description of these kinematic elements that explain their utility in the model is presented next.

At relatively high velocities, the ice fails in a brittle manner, and therefore, the deformation of ice is purely elastic. This local elastic deformation is captured by the front

non-linear spring element with stiffness K_2. Additionally, it accounts for the local brittle fracture of ice that occurs when the pre-defined critical deformation δ_f is reached in the front spring. Upon reaching the critical deformation δ_f, given by Equation 2.2, the element fails and is removed from the model.

$$u_{i,2} - u_{i,1} = \delta_f \tag{2.2}$$

The removed (or fractured) element is then replaced by a new element which is repositioned relative to the structure with a uniformly distributed offset value U:

$$u_{i,1} = u_{i,2} = u_{i,3} = u_s(t) - U(0, r_{max}) \tag{2.3}$$

where r_{max} is the maximum offset of an element with respect to the position of the structure.

The linear spring-dashpot combination in the middle, with damping coefficient C_1 and spring stiffness K_1, mimics the delayed-elastic deformation of ice. The combination reproduces the visco-elastic behaviour of ice in the transitional regime of velocities. This behaviour, for example, can be observed around the transition from creep to crushing, where the visco-elastic deformation delays the failure in the local contact zone and allows for a larger global load to develop. The combined K_2, K_1 and C_1 constitutes the crushing elements.

The rear non-linear dashpot with damping coefficient C_2 simulates the power-law creep deformation at very low ice sheet velocities. The viscous dashpot limits the failure of element below a certain ice velocity, which in this ice model is chosen to be the transition velocity.

2.2.2. EQUATION OF MOTION

As illustrated in Figure 2.4, each ice element has three degrees of freedom $u_{i,1}$, $u_{i,2}$ and $u_{i,3}$, for which the equations of motion are given by:

$$\begin{aligned}
u_{i,1} &= \begin{cases} u_{i,2}, & u_{i,1} < u_s \\ u_s, & u_{i,1} \geq u_s \end{cases} \\
\dot{u}_{i,2} &= \frac{K_2}{C_1}\left(u_{i,1} - u_{i,2}\right) + \frac{K_1}{C_1}\left(u_{i,3} - u_{i,2}\right) + v_{ice} - \frac{1}{C_2}\left(K_2\left(u_{i,2} - u_{i,1}\right)\right)^3 \\
\dot{u}_{i,3} &= v_{ice} - \frac{1}{C_2}\left(K_2\left(u_{i,2} - u_{i,1}\right)\right)^3
\end{aligned} \tag{2.4}$$

where v_{ice} is the constant ice drift velocity towards the structure and u_s is the structural displacement at ice action point. Overdots over $u_{i,2}$ and $u_{i,3}$ represents derivative with respect to the time. It is important to note that the dimension of C_2 is $[N^3 m^{-1} s]$.

The initial position of ice elements with respect to the structure is obtained from a uniform distribution U:

$$u_{i,1} = u_{i,2} = u_{i,3} = u_{s,0} - U(0, r_{max} + v_{ice}\, t_f) \tag{2.5}$$

where $u_{s,0}$ is the initial position of the structure and t_f is the time between initial contact and failure for an individual ice element at the ice velocity v_{ice}, assuming the non-moving structure. t_f is obtained by solving the Equation 2.4. The contribution of $v_{ice} t_f$

is added to ensure that the initial distribution of elements is similar to the distribution occurring during the interaction.

The global ice load F_{ice} exerted on the structure is thus given as the sum of the contribution of all individual ice elements:

$$F_{ice}(u_s, t) = \sum_{i=1}^{N} K_2 \left(u_{i,2} - u_{i,1}\right) \mathrm{H}\left(u_{i,1} - u_s\right) \tag{2.6}$$

where H is the Heaviside step function indicating contact or no-contact between an ice element and structure, and N is total number of ice elements.

2.2.3. MODEL INPUT PARAMETERS

The ice model described in previous section requires the definition of seven input parameters, viz. N, K_1, K_2, C_1, C_2, δ_f and r_{max}. Due to the phenomenological nature of the model, these parameters are derived from the experimental or full-scale measurements of ice action against the rigid structures; where these measurements are referred to as "reference measurement". Under the assumption that the ice behaviour does not change significantly with the changes in structural geometry, the reference measurements, and subsequently, the input parameters, obtained for the specific ice type and physical properties can be applied for simulations with different structures and ice conditions. The detailed description of obtaining input parameters from reference measurements is provided in Hendrikse (2017) and is not further repeated here.

The design ice thickness of 0.48m used in the study is based on the 50-year return period ice scenario observed in the open waters of Southern Baltic Sea (Gravesen and Kärnä, 2009). The global design crushing load F_G corresponding to this ice thickness is obtained based on ISO 19906 (2010):

$$p_G = C_R \left(\frac{h}{h_1}\right)^n \left(\frac{w}{h}\right)^m \tag{2.7a}$$

$$F_G = p_G \cdot h \cdot w = 2.81\mathrm{MN} \tag{2.7b}$$

where p_G is the ice pressure average over the nominal contact area in Pa, h is the design ice thickness of 0.48m, w is the diameter of tubular member at the ice-action point (refer to Chapter 4), h_1 is the reference ice thickness of 1m, m is an empirical coefficient equal to -0.16, n is an empirical coefficient whose value for the design ice thickness of 0.48m is determined from $-0.5 + h/5$, and C_R is the ice strength coefficient. In the current study, the C_R was assumed to be 1.0 MPa, based on the first-year maximum with a 50-year return period ice thickness.

The exact values of the reference measurements are confidential, and thus, only the input parameter values determined from the design crushing load F_G are presented in the Table 2.1. Leppäranta (1981) reported the maximum sea ice velocity of 0.40m/s in the Baltic Sea. However, in this study, a conservative value of 0.50m/s is used in the simulation. Moreover, the ice condition that is varied in this study is the ice drift velocity. Therefore, to capture all three regimes of ice-induced vibrations, the range of ice velocities chosen are: 0.005m/s, 0.01-0.25m/s with the steps of 0.01m/s, 0.30m/s, and 0.50m/s.

Table 2.1: Ice model input parameters adopted for the study

Parameters	N [-]	K_1 [N/m]	K_2 [N/m]	C_1 [Ns/m]	C_2 [N^3s/m]	δ_f [m]	r_{max} [m]
	45	7.51E+06	2.87E+07	2.70E+07	7.58E+17	0.004	0.006

3

AERODYNAMIC MODEL

The aerodynamic forces acting on the wind turbine blades determine the loads exerted by rotor on the tower and support structure. Therefore, for engineering purposes, it is important to have a good model that can provide accurate information about the rotor aerodynamics. Among the several methods that exist, this chapter focuses on the most commonly used method, named as Blade Element Momentum (BEM) method. First, in Section 3.1, an introduction of the classical BEM method and how it is used to determine the aerodynamics loads are presented. The focus of the current study is for the parked turbine when the wind speeds are in the range of 0 to the cut-in wind speed of the rotor. Such low wind speeds forces the rotor to operate at high tip speed ratio, that can lead to unsteady aerodynamics. In Section 3.2, a brief overview is given for the rotor's different flow states, when exposed to the unsteady environment. Lastly, in Section 3.3, the fundamentals of unsteady aerodynamics and its classification based on the time scale is discussed, whereafter an overview of the state of the art dynamic inflow engineering model is presented.

3.1. BLADE ELEMENT MOMENTUM THEORY

Blade element momentum (BEM) method is the simple, and computationally cheap method that has been used predominantly for engineering applications of wind turbine blades. The BEM theory introduced by Glauert (1935) and modified for wind turbine application combines the general momentum theory and blade element theory to determine wind turbine blade performances. The effect of induced inflow across the blades described by momentum theory is accounted for by modifying the angle of attack (AoA) at each element in the blade element theory. Thus, the blade element and momentum theory are linked together to define the induced velocity or induced AoA distribution. Once either of them are determined, then the other forces acting on the rotor can be easily obtained.

3.1.1. MOMENTUM THEORY

The axial momentum theory was first developed by Rankine (1865) and later improved by Froude (1889). The momentum theory is based on the conservation of linear mo-

mentum in control volume surrounding the rotor and its wake. It is the simplest aerodynamic model of a wind turbine in which the rotor is assumed as a homogeneous porous disc that extracts the kinetic energy from the wind. However, the ideal axial momentum theory is based on the following assumptions (Mulugeta and Gerawork (2017) & Van Der Deijl (2018)):

1. Definite streamlines exist in the flow field;
2. Flow is assumed to be entirely axial with no wake rotation;
3. Uniform loading in the azimuthal direction, which is equivalent to a rotor with an infinite number of blades (actuator disc);
4. Uniform loading in the radial direction, i.e. the pressure increment or thrust per unit area is constant over the disc

Applying the momentum theory to the control volume depicted in Figure 3.1, the following well-known expressions for wind turbine rotors are obtained:

$$C_T = 4\,a\,(1-a), \quad C_P = 4\,a\,(1-a)^2 \tag{3.1}$$

where C_T is the thrust coefficient, C_P is the power coefficient, and a is the axial induction factor.

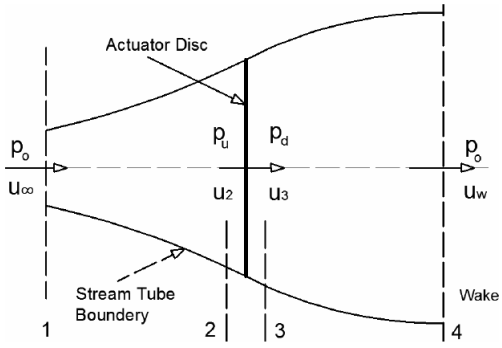

Figure 3.1: Control volume of a wind turbine (Mulugeta and Gerawork, 2017).

The axial induction factor a is the measure of the influence of the turbine on the air and is defined as the fractional decrease in the wind velocity between the free stream and the rotor plane (Mulugeta and Gerawork, 2017); planes depicted by number 2 and 3 in the Figure 3.1.

$$U_r = U_\infty\,(1-a) \tag{3.2}$$

where U_∞ is the freestream velocity or undisturbed wind speed, and U_r is the axial velocity at any point in the rotor plane.

In the initial assumption of the axial momentum theory, it was assumed that no rotation was imparted to the flow. In reality, the rotating wind turbine causes the flow behind

the rotor to rotate in the opposite direction of the rotor, in reaction to the torque exerted by the flow on the rotor. Rotational wake effect was included in the momentum theory by Betz (1920). When the wake rotation is included, the induced velocity at the rotor consists of axial component $U_\infty a$ and the tangential component U_θ given in Equation 3.3.

$$U_\theta = r\,\Omega\,a' \tag{3.3}$$

where a' is the angular induction factor, and Ω is the angular velocity (or rotational speed) of the rotor.

Using the conservation of linear and angular momentum, the incremental thrust dT_{MT} and torque dQ_{MT} acting on an annular element dr at a radial distance r from the hub is written as

$$dT_{MT} = 4\pi r\,\rho\,U_\infty^2\,a\,(1-a)\,\mathrm{dr}, \quad dQ_{MT} = 4\pi r^3\,\rho\,U_\infty\,\Omega\,(1-a)\,a'\,\mathrm{dr} \tag{3.4}$$

where ρ is the air density.

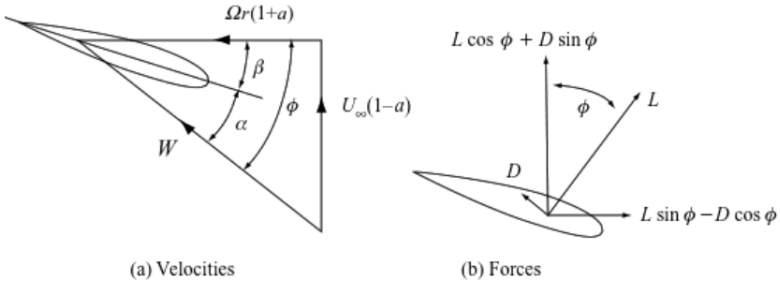

Figure 3.2: Velocity and force diagram at rotor plane (Burton et al., 2011).

3.1.2. BLADE ELEMENT THEORY

Blade element theory was first originated by Froude (1878) and later developed by Drzewiecki (1892). The momentum theory, described before, determines the thrust and torque from the change of momentum of the fluid. The blade element theory, on the other hand, is an alternative method of determining thrust and torque analytically as a function of blade geometry. The forces acting on the differential element of the blade is based on the relative velocity of the wind with respect to the rotor, as illustrated in Figure 3.2. The fundamental assumption of blade element theory is the behaviour of an element is not affected by the successive elements along the blade, and thus, the forces acting on a blade element are entirely due to the lift and drag characteristics of an airfoil (Wilson et al., 1976).

The blade is divided radially into N elements of infinitesimal length, each element representing an airfoil. Figure 3.2 depicts a cross-section of blade element, showing the sketch of flow environment. The resultant flow velocity V_{rel} (W in Figure 3.2) perceived on a blade element at a radial distance r from the centre of hub (or rotational axis) has two components: rotor's out-of-plane component V_n as a result of induced inflow velocity and in-plane component V_t due to the rotation of blade. Therefore, the normal,

tangential, and resultant velocity at a blade element is given as

$$V_n = U_\infty (1-a), \quad V_t = r\,\Omega\,(1+a'), \quad V_{rel} = \sqrt{V_n^2 + V_t^2} \tag{3.5}$$

The components of resultant flow velocity results in the force parallel and perpendicular to the flow direction; former is termed as drag force dD and latter as lift force dL, expressed as

$$dL = \frac{1}{2}\,\rho\,V_{rel}^2\,c(r)\,C_l(\alpha)\,\mathrm{d}r, \quad dD = \frac{1}{2}\,\rho\,V_{rel}^2\,c(r)\,C_d(\alpha)\,\mathrm{d}r \tag{3.6}$$

where $c(r)$ is the local chord length of the blade. $C_l(\alpha)$ and $C_d(\alpha)$ are lift and drag coefficients respectively, both as a function of AoA α. From the velocity diagram in Figure 3.2, the relationship between the inflow angle ϕ, local blade pitch θ and the angle of attack α is obtained as

$$\alpha = \phi - \theta, \quad \tan\phi = \frac{V_n}{V_t} \tag{3.7}$$

where θ is the combination of blade twist $\theta(r)$ and the constant pitch θ_o, given as $\theta = \theta(r) + \theta_o$. In stand-still operational scenario, $\theta_o = 90°$ and at maximum operation rotational speed, $\theta_o = 0°$. In the current study, the constant blade pitch is chosen as 2°.

From the force diagram in Figure 3.2, the lift and drag forces can be resolved into the axial and tangential direction, thus obtaining the elemental thrust and tangential force respectively. The thrust (dT_{BE}) and torque (dQ_{BE}) acting on a blade element on an annular rotor section as a function of inflow angles and airfoil characteristics is given by

$$dT_{BE} = N_b\left(dL\cos\phi + dD\sin\phi\right), \quad dQ_{BE} = N_b\,r\,(dL\sin\phi - dD\cos\phi) \tag{3.8}$$

where N_b is the number of blades.

3.1.3. BLADE ELEMENT MOMENTUM METHOD

The blade element momentum method (BEM) combines the basic principles of blade element and momentum theory approaches. The principle involves the invocation of equivalence between the circulation and momentum theories of lift, in other words, change in momentum over the rotor is due to the force acting on the blades (Leishman, 2016). By equating the thrust determined from the momentum theory (Eq. 3.4) and the blade element theory (Eq. 3.8), the following relationship of axial induction a can be obtained

$$\frac{a}{1-a} = \frac{\sigma\left(C_l\cos\phi + C_d\sin\phi\right)}{4\sin^2\phi}, \quad \sigma = \frac{N_b\,c}{2\pi\,r} \tag{3.9}$$

where σ is termed as rotor solidity.

Similarly, by equating the torque derived in both momentum theory (Equation 3.4) and blade element theory (Equation 3.8), provides the following relationship of tangential induction a'

$$\frac{a'}{1+a'} = \frac{\sigma\left(C_l\sin\phi - C_d\cos\phi\right)}{4\sin\phi\cos\phi} \tag{3.10}$$

The solution of a and a' are obtained using the iterative procedure for each annulus independently until the values have converged to an acceptable tolerance.

3.1.4. ENGINEERING MODIFICATIONS FOR BEM METHOD

The BEM method developed by Glauert (1935) is still used today in the industry for rotor design. However, the physical effects that are not modelled by the Glauert's theory, which are the difference between an actuator disc and a rotor with a finite number of blades, and for flow condition where the momentum theory breaks down, is further improved by employing correction methods to cope with various operating conditions of wind turbine.

FINITE NUMBER OF BLADES

One of the assumptions of the momentum theory is the azimuthally independent stream tubes that are only valid for an infinite number of blades. However, in the blade element theory, the rotor forces act on a finite number of blades, thereby leading to a concentration of loading on the blades, and the shedding of the concentrated tip and hub vortices. These concentrated vortices produce high local inflow at the tip and the root region of the blade resulting in an increased induction, commonly referred to as tip and hub losses.

In order to correct the assumption of infinite number of blades and give results that are very similar for case with finite number of blades, Prandtl derived a tip $\left(f_{tip(\mu)}\right)$ and hub $\left(f_{hub(\mu)}\right)$ correction for induction factors. These corrections are expressed as (Burton et al., 2011)

$$f_{tip(\mu)} = \frac{2}{\pi}\arccos\left(\exp\left(-\frac{N_b}{2}\frac{1-\mu}{\mu}\sqrt{1+\left(\frac{\lambda\mu}{1-a}\right)^2}\right)\right) \tag{3.11a}$$

$$f_{hub(\mu)} = \frac{2}{\pi}\arccos\left(\exp\left(-\frac{N_b}{2}\frac{\mu-\mu_{hub}}{\mu}\sqrt{1+\left(\frac{\lambda\mu}{1-a}\right)^2}\right)\right) \tag{3.11b}$$

$$\lambda = \frac{\Omega R}{U_\infty}, \quad \mu = \frac{r}{R} \tag{3.11c}$$

where μ is the non-dimensional radial position of a blade element, μ_{hub} is the location of the root region of the blade, and λ is the tip speed ratio.

The total loss factor (F) for finite number of blades at each radial position is the product of the hub-loss and tip-loss factors, which is written as

$$F = f_{tip(\mu)} \cdot f_{hub(\mu)} \tag{3.12}$$

Thus, in the BEM method, the Equations 3.9 and 3.10 takes the form as

$$\frac{a}{1-a} = \frac{\sigma\left(C_l\cos\phi + C_d\sin\phi\right)}{4F\sin^2\phi}, \quad \frac{a'}{1+a'} = \frac{\sigma\left(C_l\sin\phi - C_d\cos\phi\right)}{4F\sin\phi\cos\phi} \tag{3.13}$$

HEAVILY LOADED ROTORS

The momentum theory is considered valid for the small expansion of wake, and therefore, the theory breaks down when the axial induction factor becomes larger than approximately 0.3-0.4 (Mulugeta and Gerawork, 2017). Figure 3.3 shows the different flow states of the rotor (described in detail in Sec. 3.2) and the range of axial induction for

which the momentum theory is valid. The rotor operating at large values of the axial induction factor is generally referred to as heavily loaded rotors.

The break down of momentum theory usually occurs at high tip speed ratio, when the turbine wake enters the "turbulent wake state". An empirical relationship between the axial induction and thrust coefficient proposed by Glauert (1935) is used to extend the range of validity of BEM model. The Equation 3.1 is modified to (Burton et al., 2011)

$$C_T = \begin{cases} 4\,a\,(1-a), & a < 1 - \dfrac{\sqrt{C_{T1}}}{2} \\ C_{T1} - 4\left(\sqrt{C_{T1}} - 1\right)(1-a), & a \geq 1 - \dfrac{\sqrt{C_{T1}}}{2} \end{cases} \tag{3.14}$$

where $C_{T1} = 1.816$.

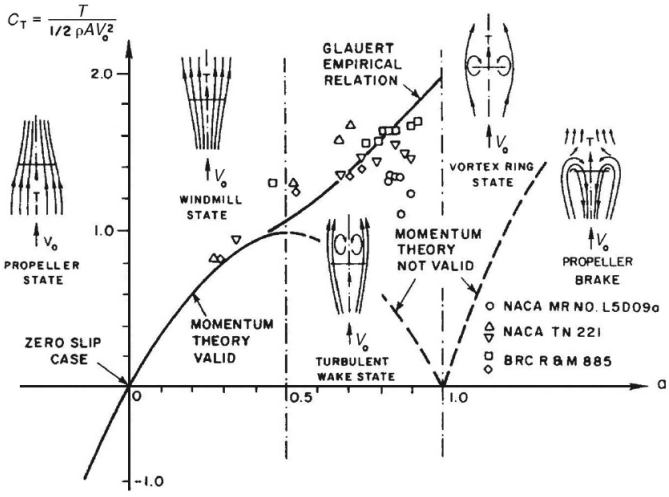

Figure 3.3: Measured thrust coefficient C_T as a function of axial induction factor a showing various rotor flow states (Burton et al., 2011).

3.2. FLOW STATES

In normal operating condition, the flow is steady, and the wind turbine rotor operates in the "windmill state", extracting energy from the flow field. In reality, due to the presence of unsteady aerodynamics (described in Sec. 3.3), the rotor can enter different flow states depicted in Figure 3.3, which can be easily identified based on the simple actuator disc theory (Sørensen et al., 1998).

- *Propeller state*: Rotor adds kinetic energy to the flow and therefore needs to be powered. This state has negative induction factor ($a < 0$) and thrust coefficient ($C_T < 0$), thus thrust opposes the flow. The general momentum theory is still valid; however, the wind turbine acts as a propeller.
- *Windmill state*: Kinetic energy is extracted from the flow and thus drives the rotor. This state is the usual operating condition of a wind turbine in which the range of

induction factor is $0 < a \leq 0.5$ and momentum theory described earlier in Sec. 3.1.1 is valid.

- *Turbulent wake state*: The wake state appears for $0.5 \leq a \leq 1$, in which the rotor yields flow reversal in the wake, resulting in the recirculating flow in the downstream of the rotor. While the general momentum theory no longer describes the behaviour of a wind turbine, the Glauert (1935) empirical relation for heavily loaded rotors is often used for the rotor design.

- *Vortex ring state*: For values of a not greatly over unity, the flow near the disc resembles vortex rings, and the rotor enters the vortex ring state. It occurs at high tip speed ratio, and the general momentum theory breaks down entirely. As the rotor sheds energy into the flow, its behaviour approaches that of a propeller.

- *Propeller break state*: For $a > 1$, the rotor reverses the direction of the flow with the power being added to the flow, and the downwind thrust is created.

The rotor goes from the windmill state to the turbulent wake state or vortex ring state at high tip speed ratio; for a constant wind speed that means at a higher rotational speed of the rotor. At this point, it is important to note here that these flow states are essential for the current study as it is highly likely that the wind turbine operating at different rotational speeds below cut-in speed can enter these four flow states.

3.3. UNSTEADY AERODYNAMICS

Owing to the simplicity of the BEM model, it is the most popular engineering model for predicting the performance and the load distribution of the horizontal axis wind turbine. The main intrinsic assumption of the BEM model is that it only holds in a steady flow. The equilibrium state of momentum equation assumes that a change in the force and the wake is instantaneous, i.e. no time lag due to the airfoil aerodynamics and the wake dynamics on the rotor (Van Der Deijl, 2018). However, in reality, the environments in which wind turbines operate, such as wind shear, atmospheric turbulence, and motions and vibrations of structures are by its nature unsteady. As a result, the wake and the induced velocities can no longer be treated in steady or quasi-steady sense.

Unsteady aerodynamics can be divided into mainly two parts, namely unsteady profile aerodynamics and dynamic inflow (Snel and Schepers, 1992). The first part takes into account the sectional aerodynamics forces on the time-varying angle of attack. Since this part introduces time lag in airfoil forces, the characteristic time scale associated with this dynamic effect is proportional to the ratio of the chord to the effective velocity seen by the blade, approximately $c/(\Omega r)$, typically in the order of a fraction of seconds (Vaal et al., 2014). The indicator for aerodynamic unsteadiness due to the profile aerodynamics is the reduced frequency analysis k. For the values of $k > 0.05$, the flow is classified as unsteady.

$$k = \frac{\Omega c}{2V} \tag{3.15}$$

The dynamic inflow part takes into account the change in wake configuration and induced velocities due to the changes in rotor loading. In the BEM model, it is assumed

that the inflow is always in equilibrium with the loads. In reality, however, it takes time to accelerate the mass of air flowing through the rotor, and therefore, the flow takes time to adjust to a new equilibrium. This means that the flow and the forces gradually reach the equilibrium; thus resulting in an induced velocity with time delay. The characteristic time scale associated with this phenomenon is D/U, typically in the order of 5 to 20s for modern wind turbines (Vaal et al., 2014). The unsteady aerodynamic due to the wake is represented by a non-dimensional parameter introduced by Bayati et al. (2017) known as the "wake reduced velocity" V_w^*. At high values of V_w^*, the flow behaves in a quasi-steady manner. On the other hand, for the low values of V_w^*, rotor operates in unsteady aerodynamics.

$$V_w^* = \frac{V}{fD} \tag{3.16}$$

where f is the structural motion frequency, and D is the rotor diameter.

Out of the two unsteady aerodynamic effects, the dynamic inflow has the time scale in the comparable order of magnitude as the natural period of the structural motion and therefore in the current study we choose to focus on the wake dynamics only.

3.3.1. STIG ØYE DYNAMIC INFLOW MODEL

Several engineering models have been devised to account for unsteady dynamic inflow effect into BEM model and are discussed by Snel and Schepers (1992). Of these engineering models, the most commonly used is the one proposed by Stig Øye, presented in the Snel and Schepers (1995) and the book of Hansen (2015). In this model, the dynamic effect is simulated by passing the quasi-steady induced velocities, determined from the standard BEM method, through two first-order differential equations. The model is written into the following set of differential equations:

$$\underline{W}_{qs} + 0.6\tau_1 \frac{d\underline{W}_{qs}}{dt} = \underline{W}_{int} + \tau_1 \frac{d\underline{W}_{int}}{dt}, \qquad \underline{W}_{int} = \underline{W} + \tau_2 \frac{d\underline{W}}{dt} \tag{3.17}$$

where $\underline{W}$ is the dynamically adjusted induced velocity at the rotor, $\underline{W}_{qs}$ is the quasi-steady induced velocity, and $\underline{W}_{int}$ is an intermediate value. Within the implementation of unsteady BEM model, as described in Hansen (2015), the quasi-steady induced velocity vector is determined according to Equation 3.18, once the induction a and a' are known from the standard BEM method.

$$\underline{W}_{qs} = -a \begin{pmatrix} 0 \\ U_o \end{pmatrix} - a' \begin{pmatrix} \Omega r \\ 0 \end{pmatrix} \tag{3.18}$$

The two time constants in the Equation 3.17 are calibrated using a discrete vortex ring models and are written as

$$\tau_1 = \frac{1.1}{1 - 1.3\min(a, 0.5)} \frac{R}{U_o}, \qquad \tau_2 = \left(0.39 - 0.26 \frac{r^2}{R^2}\right) \tau_1 \tag{3.19}$$

where R is the rotor radius.

At any time instant, the relative velocity seen by the blade presented in Equation 3.5 is replaced by the Equation 3.20, which includes time dependent induced velocity $\underline{W}$ and

the tower displacement $\dot{u}$.

$$\underline{V}_{rel} = \begin{pmatrix} 0 \\ U_o \end{pmatrix} + \begin{pmatrix} \Omega r \\ 0 \end{pmatrix} - \begin{pmatrix} 0 \\ \dot{u} \end{pmatrix} + \underline{W} \tag{3.20}$$

The numerical implementation of Equation 3.17 into the steady BEM model is presented by Hansen (2015) and is therefore not replicated here.

4

APPROACH AND MODELLING

In Chapter 2, the phenomenological ice model was explained for simulating dynamic ice-structure interaction. Next, in Chapter 3, the steady BEM model was discussed and extended to unsteady aerodynamics, that accurately predicts the aerodynamic loads exerted by the rotor on the support structure. This chapter demonstrates the approach adopted to model the aero-ice-structure interaction to an offshore wind turbine in a realistic manner.

First, in Section 4.1, the various components of a typical offshore wind turbine are defined which was originally designed in the UpWind project. Next, in Section 4.2, the formulation of a multi-degree-of-freedom structural model undergoing lateral vibration in the fore-aft direction is treated and implemented into the MATLAB. To achieve this, the Finite Difference method (FDM) modelling technique was adopted. In Section 4.3, a brief overview of the solution technique known as Modal Analysis is presented for obtaining the structural response. Ultimately, in Section 4.4, the method to obtain the fatigue damage is presented, which is used as a measure to quantify the effect of control idling in mitigating the ice-induced vibrations.

4.1. STRUCTURAL MODEL

A typical offshore wind turbine can be divided into 3 components, viz. support structure, tower and rotor-nacelle assembly (RNA). A schematic representation of a typical offshore wind turbine is depicted in Figure 4.1. The support structure and tower were modelled with the Euler-Bernoulli beam elements. RNA, on the other hand, was modelled as a rigid structure implying the blade bending vibrations were not taken into account in the current study. Each beam element is associated with single degree-of-freedom (DOF) in the transversal direction; in other words, fore-aft motion only. The information on these three components that is relevant to the current study is presented in the following sections.

4.1.1. TOWER AND SUPPORT STRUCTURE

The configuration of the tower and support structure is documented in the UpWind project (Vries, 2011), hereafter referred to as the reference structure. It must be em-

phasized here that the focus of the study is to understand aero-ice-structure interaction process and not to develop an exact offshore wind turbine model. Therefore, to introduce simplicity in the structural model, the following modifications were made to the reference structure.

- Tower diameter and thickness is assumed to be constant along the length of the tower. The average diameter of the tower in the UpWind project is considered as the constant tower diameter in the structural model;
- The tower base is connected to the transition piece at an elevation of 14m above mean sea level (MSL). Further to it, the transition piece extends until 6m below MSL;
- Transition piece diameter is assumed to be the same as monopile diameter;
- Lastly, the thickness of tower, transition piece and monopile is determined based on the weight of individual component, presented in the UpWind project.

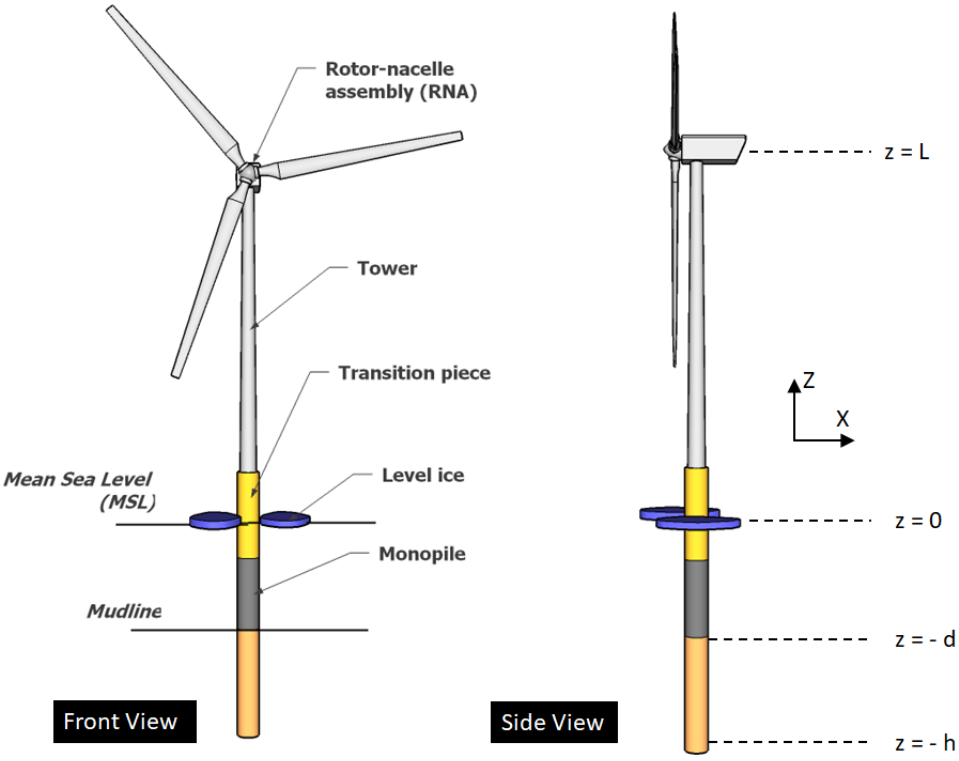

Figure 4.1: Schematic representation of an offshore wind turbine in level ice conditions.

In the fore-aft direction, the monopile was constrained in the soil through distributed lateral soil springs with constant stiffness. The stiffness value was derived from Det

Norske Veritas (2013) standard assuming the sand profile, with the 30° angle of friction, throughout the embedded length. Additionally, the monopile was assumed to have pinned connection at the bottom. The choice of pinned connection stems from Hendrikse (2017), in which he has found that the restraint on the displacement is necessary to describe the displacement shape of the structure under ice loading. All the system matrices describing the dynamic characteristics of the model were assumed to be time-independent. Table 4.1 presents the dimensions of tower and support structure along with the distributed soil stiffness value and water depth.

Table 4.1: Tower and Support structure properties

Description	Value	Unit	Description	Value	Unit
General properties			***Transition piece***		
Steel density	7,850	kg/m^3	Length above MSL	14.00	m
Water density	1,025	kg/m^3	Length below MSL	6.00	m
Water depth (MSL)	26	m	Diameter	5.75	m
Soil stiffness	100	MPa	Thickness	0.05	m
Tower			***Monopile***		
Length	68.00	m	Length above seabed	20.00	m
Diameter	4.60	m	Length below seabed	24.00	m
Thickness	0.03	m	Diameter	5.75	m
			Thickness	0.09	m

4.1.2. ROTOR AND NACELLE ASSEMBLY

The wind turbine used in the study is a representative utility-scale multi-megawatt turbine known as "NREL 5-MW baseline wind turbine", hereafter referred to as a reference wind turbine. This turbine, defined by Jonkman et al. (2009), is a conventional three-bladed upwind variable-speed variable blade-pitch-to-feather-controlled turbine and its important specifications are presented in the Table 4.2. For simplicity, RNA was modelled as a lumped mass, thereby excluding the dynamics of the blades.

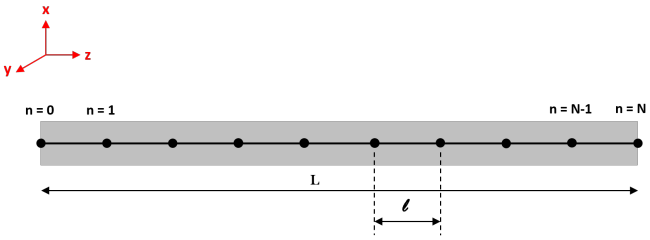

Figure 4.2: Discretization of a beam of length L. l and n denotes the length of the discretized beam and nodal points, respectively.

Table 4.2: Reference turbine specification

Description	Value
Rotor, Hub diameter	126m, 3m
Cut-in, Rated, Cut-out wind speed	3m/s, 11.4m/s, 25m/s
Cut-in, Rated Rotor speed	6.9rpm, 12.1rpm
Rotor mass	110,000kg
Nacelle mass	240,000kg
Control	Variable speed, Collective pitch

4.2. FINITE DIFFERENCE MODEL

The tower and support structure were discretized into "N" finite Euler-Bernoulli beam elements having "$N+1$" nodes. Each node was associated with one transversal DOF, viz. the fore-aft motion. Typical discretization of a beam with length L is depicted in Figure 4.2.

The governing equations of motion describing the fore-aft bending vibrations of the structural model are given by the following Partial Differential Equations (PDE). Refer to Figure 4.1 for the definition of vertical coordinates z in the equations.

$$EI_1 \frac{\partial^4 u_1}{\partial z^4} + \frac{\partial}{\partial z}\left(T_1(z)\frac{\partial u_1}{\partial z}\right) + \rho A_1 \frac{\partial^2 u_1}{\partial t^2} + K_1 u_1 = 0, \qquad -h \le z \le -d \tag{4.1a}$$

$$EI_2 \frac{\partial^4 u_2}{\partial z^4} + \frac{\partial}{\partial z}\left(T_2(z)\frac{\partial u_2}{\partial z}\right) + (\rho A_2 + \mu_2)\frac{\partial^2 u_2}{\partial t^2} = 0, \qquad -d \le z \le 0 \tag{4.1b}$$

$$EI_3 \frac{\partial^4 u_3}{\partial z^4} + \frac{\partial}{\partial z}\left(T_3(z)\frac{\partial u_3}{\partial z}\right) + \rho A_3 \frac{\partial^2 u_3}{\partial t^2} = 0, \qquad 0 \le z \le L \tag{4.1c}$$

where i = 1,2,3 representing the different parts of the structure, u_i is the displacement in positive x-direction representing the DOF of the continuous beam, EI_i is the bending stiffness, ρ is the mass density of steel, A_i is the cross-sectional area of tubular members, K_1 is the constant linear soil stiffness, and μ_2 is the added mass of the underwater part of the structure.

$T_i(z)$ in Equation 4.1b is the axial compressive force along the length of the structure that accounts for the loss of stiffness due to the compression softening, given by

$$T_i(z) = M_{top}\, g + \rho A_i\, g\, (L - z) \tag{4.2}$$

where M_{top} is the total mass of RNA, g is the gravitational constant, and z is the vertical coordinates along the length of the structure. A detailed formulation of the governing equations and the boundary conditions are given in Appendix A.

It is important to note here that the aerodynamic drag force acting on part three was ignored in this study since the tower and transition piece above water experiences low wind speed, in range of zero to cut-in wind speed, and therefore the drag force generated

by these tubular members is significantly small in comparison to the RNA aerodynamic force. Additionally, the drag force due to current on part two, i.e. underwater part of the structure, was neglected too, since the vibrations induced by the current are insignificant as compared to the ice-induced vibrations. To sum up, the focus of this study is to investigate the effect of rotor aerodynamics on ice-induced vibrations and therefore all other external forces were neglected in the study.

4.2.1. FINITE DIFFERENCE METHOD

To develop a structural model of a multi-degree-of-freedom structure, one needs to obtain the mass and stiffness matrix from the PDEs. One of the methods is the spatial discretization of PDEs using Finite Difference method (FDM). It is a powerful numerical technique to solve the differential equations with generalized end conditions. FDM converts the PDE into a set of an ordinary differential equation (ODE), which then can be solved numerically using an ODE solver. The basis of this method is to approximate the function derivatives with Taylor series expansion. In this study, among the different schemes in FDM, the central difference scheme (CDM) was adopted to discretize the continuous PDE spatially.

The formulation of spatial derivative in terms of spatial coordinates with second order accuracy $\mathcal{O}(l^2)$ was derived by Fornberg (1988) and is reproduced in Appendix A. Among all the spatial derivatives presented in Equation 4.1, various approaches have been employed in the literatures for the spatial discretization of the second term from left. In the current study, the discretization derived by Salani and Matlock (1967) was adopted and is shown below.

$$\begin{aligned}\frac{\partial}{\partial z}\left(T(z)\,\frac{\partial u_n}{\partial z}\right) &\approx \frac{1}{l}\left[-\frac{1}{2}\left(T(z)\,\frac{\partial u}{\partial z}\right)_{n-1}+\frac{1}{2}\left(T(z)\,\frac{\partial u}{\partial z}\right)_{n+1}\right]+\mathcal{O}(l^2)\\ &\approx \frac{1}{4\,l^2}\left(T_{n-1}(z)\,u_{n-2}-\Big(T_{n-1}(z)+T_{n+1}(z)\Big)\,u_n+T_{n+1}(z)\,u_{n+2}\right)+\mathcal{O}(l^2)\end{aligned} \tag{4.3}$$

By substituting the spatial derivatives in terms of nodal displacements into the governing equation of motions (Equation 4.1), along with the end conditions described in Appendix A, the PDE in time and space domain is translated into the time domain ODE. Assembling the coefficients of nodal accelerations and displacements yield the following system of "N" equations of motion:

$$\mathbf{M}\ddot{\mathbf{u}}(t)+\mathbf{C}\dot{\mathbf{u}}(t)+\mathbf{K}\mathbf{u}(t)=\mathbf{f}(t) \tag{4.4}$$

where the structure's mass and stiffness matrices are denoted by $(\mathbf{M},\mathbf{K})\in\mathbb{R}^{N\times N}$ respectively, and the force vector is represented by $\mathbf{f}(t)\in\mathbb{R}^N$. The damping matrix $\mathbf{C}\in\mathbb{R}^{N\times N}$ represents the structural damping described in the next section.

4.2.2. STRUCTURAL DAMPING

The structural damping in the current Finite Difference (FD) model is represented by Rayleigh Damping, which is the linear combination of mass and stiffness matrix, defined as

$$\mathbf{C}=\alpha_1\mathbf{M}+\alpha_2\mathbf{K} \tag{4.5}$$

where α_1 and α_2 are proportionality constants.

Due to the orthogonality of eigenvectors with respect to the mass and stiffness matrices, the damping matrix obtained by Rayleigh Damping model is orthogonal too with respect to eigenvectors. Using this orthogonality condition, the modal damping ratio ξ_i as a function of eigenfrequency ω_n (determined in Sec. 4.2.3) and the proportionality constants were derived by Spijkers et al. (2005), which is given in Equation 4.6.

$$\xi_i = \frac{\alpha_1}{2\omega_i} + \frac{\alpha_2}{2}\omega_i \tag{4.6}$$

α_1 and α_2 are usually obtained by presuming the damping ratio ξ_i of the first two principal modes, which in the current study was taken as 1% of critical, or 0.01 (Valamanesh and Myers, 2014). A plot of damping ratio variation with first six natural frequencies is depicted in Figure 4.3, in which it can be seen that higher modes are significantly damped.

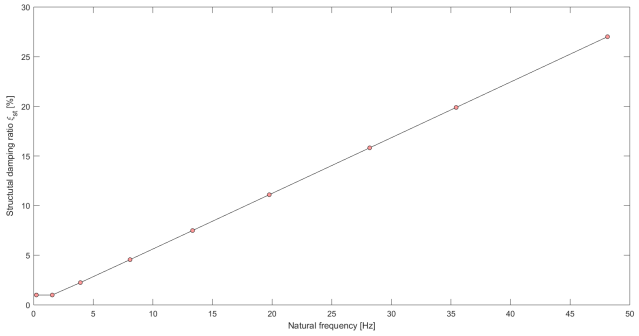

Figure 4.3: Structural damping ratio variation with the natural frequency of the system.

4.2.3. EIGENVALUES AND EIGENMODES

The eigenanalysis gives insight into the characteristic behavior of the structure via the eigenvalues and eigenvectors; ergo providing the information of the natural frequencies and the modal shapes of the structure. With the help of global mass and stiffness matrices obtained in Sec. 4.2.1, the generalized eigenvalue problem is expressed as

$$\left(\mathbf{K} - \omega^2 \mathbf{M}\right)\mathbf{\Phi} = 0 \tag{4.7}$$

where $\omega \in \mathbb{R}^N$ is the natural frequencies of the system, ω^2 represents the eigenvalue, and $\mathbf{\Phi} \in \mathbb{R}^{N\times N}$ is the matrix containing the eigenvectors of the undamped system. The Equation 4.7 is computed directly by employing *"eig"* function handle in MATLAB.

The FD model was validated by comparing the natural frequencies with the UpWind monopile design results (Vries, 2011). Table 4.3 shows the comparison of the first two natural frequencies that correspond to the fore-aft bending modes.

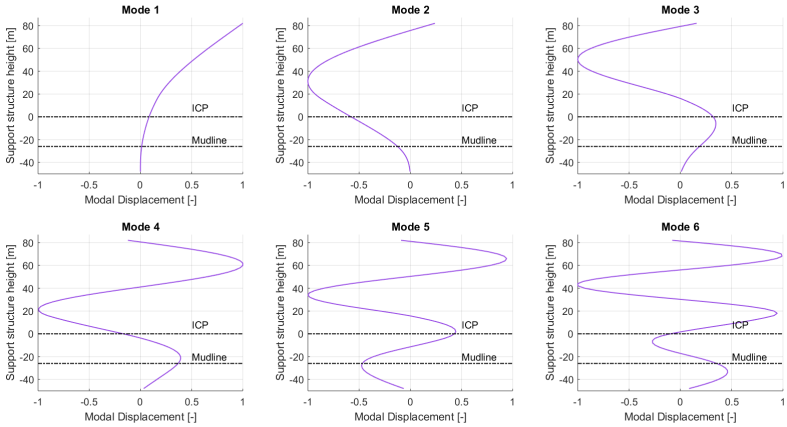

Figure 4.4: Normalized mode shapes of FD model; *ICP* is Ice-action point.

Table 4.3: Natural frequency comparison between FD model and UpWind project

Description	FD Model [Hz]	UpWind [Hz]	Difference [%]
1st fore-aft bending frequency	0.224	0.277	19.13
2nd fore-aft bending frequency	1.558	1.290	20.78

The difference in natural frequencies is attributed to the following reasons:

1. The first mode shape is sensitive to the soil-pile interaction and thus, the simplifications and assumptions taken in modelling soil-pile interaction, described in Sec. 4.1.1, has a significant influence on its natural frequency. In comparison, the UpWind project has non-uniform soil throughout the seabed which are modelled using more realistic P-Y curves;

2. The second mode shape experiences large deformation at the location of the transition piece, and thus its properties such as the mass and stiffness has a significant influence on the natural frequency. On the contrary, in the UpWind project, the transition piece was connected to the top of the monopile through grouted connection. The grouted connection makes the structure stiffer and increases the local mass, and thereby, affects the natural frequency.

To this end, the developed FD model was deemed sufficiently accurate to study the ice-induced vibrations as it still captures the essential dynamic characteristics of the structure.

Figure 4.4 illustrates the first six fore-aft normalized bending mode shapes of the structure; modes were normalized with respect to the corresponding maximum modal displacements. The ice interaction takes place at the ice-action point (ICP) situated at z = 0m and aerodynamic loading acts at the tower top situated at z = 82m. The modal amplitudes at these locations determine the significance of the modes in ice-induced

vibrations. Higher modal amplitude implies that the corresponding mode can extract energy relatively easy from the forcing. Table 4.4 presents the natural frequencies, structural damping ratios and the normalized modal amplitudes for the mode shape shown in Figure 4.4.

Table 4.4: Dynamic characteristics of the structural model

Mode shape	Natural frequency [Hz]	Damping ratio [%]	Modal amplitude [-]	
			ICP [1]	Tower top
1	0.224	1.00	0.08	1.00
2	1.558	1.00	0.58	0.24
3	3.919	2.25	0.32	0.16
4	8.084	4.56	0.17	0.12
5	13.327	7.49	0.43	0.09
6	19.763	11.10	0.10	0.08

[1] *ICP* is Ice-action point.

FREQUENCY RESPONSE FUNCTION

To better understand the susceptibility of eigenmodes to an applied force at a certain DOF, the frequency response function (FRF) analysis is often used. The FRF represents the relation between the response at a DOF m due to the loading at DOF n. The response that is of interest in the current study is the displacements at tower top and ice-action point, and the load acting is the global ice force at the MSL. This is done by employing the standard linear inverse problem, defined in Equation 4.8.

$$\mathbf{A}\mathbf{x} = \mathbf{b} \tag{4.8}$$

where $\mathbf{x} \in \mathbb{R}^N$ and $\mathbf{b} \in \mathbb{R}^N$ are the vectors describing the force, and the displacement respectively. The matrix $\mathbf{A} \in \mathbb{R}^{N\times N}$ relates the displacement to the force, and thus, is nothing more than the FRF $\tilde{\mathbf{H}}(\omega)$, which takes the form in frequency domain as given below.

$$\tilde{\mathbf{H}}(\omega) = \left(\mathbf{M}\omega^2 + i\omega\mathbf{C} + \mathbf{K}\right)^{-1} \tag{4.9}$$

The FRF is multiplied by the force and displacement selection matrix to obtain the response function matrix, $\mathbf{R}(\omega) \in \mathbb{R}^{m\times n}$.

$$\mathbf{R}(\omega) = \mathbf{S}_d\,\tilde{\mathbf{H}}(\omega)\,\mathbf{S}_p \tag{4.10}$$

where $\mathbf{S}_d \in \mathbb{R}^{m\times N}$ is the displacement selection matrix, $\mathbf{S}_p \in \mathbb{R}^{N\times n}$ is the force selection matrix, N is the number of DOFs, n is the number of forces (equal to 1), and m is the number of output responses (equals to 2). In Figure 4.5, $\mathbf{R}(\omega) \in \mathbb{R}^{1\times 1}$ and $\in \mathbb{R}^{2\times 1}$ for the range of frequencies are plotted, where the former relates the response at ice action point and latter relates the response at the tower top due to the ice action at MSL.

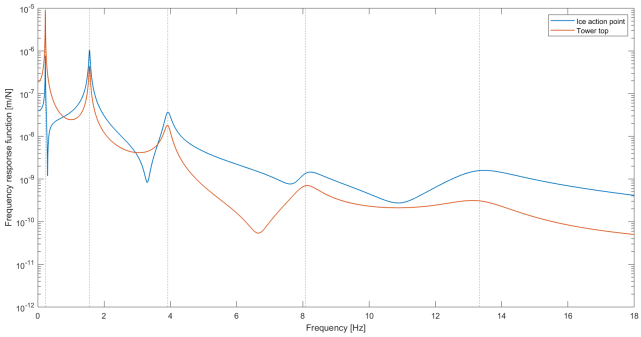

Figure 4.5: Frequency response function. Vertical dashed lines indicate the first five eigenfrequencies.

By comparing the Figure 4.5 and the modal amplitudes presented in Table 4.4, the following deductions can be made:

1. For the response at the ice-action point, the excited modes are first and second. Looking into the Table 4.4, even though the modes three and five have higher amplitudes, these modes are relatively less excited due to the presence of higher damping ratio;

2. And at the tower top, the first mode is excited the most with the reduction in response at higher modes due to the higher modal damping and relatively low modal amplitudes.

Thus, it can be concluded from Table 4.4 and Figure 4.5, that the majority of ice-induced response will occur in the first and second bending mode of vibrations.

4.3. MODAL ANALYSIS

The structural response of a free vibration system is the summation of all eigenmodes (Spijkers et al. (2005)). In the modal analysis, these eigenmodes form a complete basis to describe the dynamic behaviour of the system. The displacement $\mathbf{u}(z,t)$ is, therefore, written as the linear combination of the products between the $\mathbf{\Phi}$, accounting for spatial variations, and $\boldsymbol{\eta}(t)$, accounting for the time dependence.

$$\mathbf{u}(z,t) = \mathbf{\Phi}\,\boldsymbol{\eta}(t) \tag{4.11}$$

where $\mathbf{\Phi}$ was determined in Equation 4.7 and $\boldsymbol{\eta}(t) \in \mathbb{R}^N$ is the modal displacement vector.

Substituting Equation 4.11 into the Equation 4.4 and pre-multiplying by the transpose of the eigenvectors $\mathbf{\Phi}^T$, yields the following:

$$\underbrace{\mathbf{\Phi}^T\mathbf{M}\mathbf{\Phi}}_{\mathbf{M}^*}\ddot{\mathbf{u}} + \underbrace{\mathbf{\Phi}^T\mathbf{C}\mathbf{\Phi}}_{\mathbf{C}^*}\dot{\mathbf{u}} + \underbrace{\mathbf{\Phi}^T\mathbf{K}\mathbf{\Phi}}_{\mathbf{K}^*}\mathbf{u} = \underbrace{\mathbf{\Phi}^T\mathbf{f}}_{\mathbf{f}^*} \tag{4.12}$$

Due to the orthogonality of eigenvectors with respect to the mass and stiffness, the resulting modal mass ($\mathbf{M}^*$) and stiffness ($\mathbf{K}^*$) matrices are diagonal. Furthermore, since

the damping matrix $\mathbf{C}$, determined in Sec. 4.2.2, is the linear combination of mass and stiffness matrix, the resulting modal damping matrix $\mathbf{C}^*$ is diagonal as well. Thus, the coupled system of equations (Equation 4.4) simplifies to the decoupled set of differential equations, given by

$$\mathbf{M}^* \ddot{\boldsymbol{\eta}}(t) + \mathbf{C}^* \dot{\boldsymbol{\eta}}(t) + \mathbf{K}^* \boldsymbol{\eta}(t) = \mathbf{f}^* \tag{4.13}$$

where the modal mass, damping and stiffness matrices are described in Appendix A.

4.3.1. REDUCED ORDER MODEL

The great strength of the modal analysis is that model can be reduced into the truncated set of modal coordinates which can still approximate the true model with good accuracy. Since the higher eigenmodes contribution is less dominant, as discussed in Sec. 4.2.3, these eigenmodes can be easily neglected from the analysis; thereby provides considerable aid in reducing the computational time. The system, therefore, can be approximated to a set of reduced modal coordinates, as follows:

$$\mathbf{u}(z,t) \approx \boldsymbol{\Phi}_r \boldsymbol{\eta}_r = \mathbf{u}_r \tag{4.14}$$

in which $\boldsymbol{\Phi}_r \in \mathbb{R}^{N \times n_r}$ is the reduced order matrix containing n_r eigenvectors. The reduced order modal displacement vector is represented by $\boldsymbol{\eta}_r \in \mathbb{R}^{n_r}$, where $1 \leq n_r \leq N$ are the number of retained modes. In order to include the effect of higher modes in the truncated response, the number of retained eigenmodes chosen for the analysis were five. Similar to Equation 4.12, the reduced set of equation of motions is expressed as

$$\underbrace{\boldsymbol{\Phi}_r^T \mathbf{M} \boldsymbol{\Phi}_r}_{\mathbf{M}_r^*} \ddot{\boldsymbol{\eta}}_r(t) + \underbrace{\boldsymbol{\Phi}_r^T \mathbf{C} \boldsymbol{\Phi}_r}_{\mathbf{C}_r^*} \dot{\boldsymbol{\eta}}_r(t) + \underbrace{\boldsymbol{\Phi}_r^T \mathbf{K} \boldsymbol{\Phi}_r}_{\mathbf{K}_r^*} \boldsymbol{\eta}_r(t) = \underbrace{\boldsymbol{\Phi}_r^T \mathbf{f}}_{\mathbf{f}_r^*} \tag{4.15}$$

4.3.2. STATE SPACE REPRESENTATION

The state-space transformation allows rewritting the modal displacement and velocity in terms of the modal state space vector $\mathbf{x}(t) \in \mathbb{R}^{2n_r}$, which is given as (Lourens et al., 2012)

$$\mathbf{x}(t) = \begin{bmatrix} \boldsymbol{\eta}_r(t) \\ \dot{\boldsymbol{\eta}}_r(t) \end{bmatrix} \tag{4.16}$$

Substituting Equation 4.16 into reduced order equation of motion 4.15 yields the first-order continuous-time state equation, given by Lourens et al. (2012)

$$\dot{\mathbf{x}}(t) = \mathbf{A}_c \mathbf{x}(t) + \mathbf{B}_c \mathbf{f}(t) \tag{4.17}$$

where the system matrices $\mathbf{A}_c \in \mathbb{R}^{n_r \times n_r}$ and $\mathbf{B}_c \in \mathbb{R}^{n_r \times N}$ are defined as

$$\mathbf{A_c} = \begin{bmatrix} \mathbf{0} & \mathbf{I} \\ -\mathbf{M_r^{*-1}} \mathbf{K_r^*} & -\mathbf{M_r^{*-1}} \mathbf{C_r^*} \end{bmatrix}; \quad \mathbf{B_c} = \begin{bmatrix} \mathbf{0} \\ \mathbf{M_r^{*-1}} \boldsymbol{\Phi}_r^T \end{bmatrix}$$

The above first order reduced state-space modal equation 4.17 is then solved easily in MATLAB by the application of 4th order Runge-Kutta method "ODE45".

4.4. FATIGUE DAMAGE

In the current study, the measure of fatigue damage is used to quantify the potential effect of control idling in mitigating the ice-induced vibrations. Fatigue damage is a convenient choice since it is a design driving factor in the offshore wind turbine. The aim of fatigue analysis is to ensure that the structure, which is subjected to extensive dynamic loading, fulfil its intended function for the design lifetime. Usually, for the monopile design, the bending moment has the highest contribution on the total stresses, and therefore, the critical location chosen for the fatigue damage evaluation was at the mudline.

4.4.1. STRESS DISTRIBUTION

The stresses that are important for the analysis of a structural cross-section are normal and shear stresses; the normal stress being the summation of stresses from the axial load and bending moment. A typical cross-section of a tubular member is depicted in Figure 4.6.

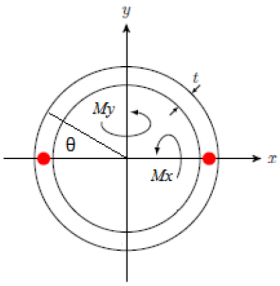

Figure 4.6: Cross-section of a tubular member, where the angle θ denotes the location at which stresses are evaluated. Maximum fatigue damage is expected to occur at red spot, i.e. $\theta = 0°$or $180°$.

For ice and aerodynamics forces acting in the x-direction, the generalized normal stress σ_N, presented by Li et al. (2018), is simplified to stresses due to the axial force and the in-plane bending moment only, i.e. $\theta = 0°$. The shear stress τ_{xy} used in the analysis was proposed by Hoogenboom and Spaan (2005).

$$\sigma_N = \frac{N_z}{A} \pm \frac{M_y}{I_y} R_m, \quad \tau_{xy} = \frac{V}{0.5\,A} \tag{4.18}$$

where A is the nominal cross-section area, R_m is the mean cross-section radius, N_z is the axial force, M_y is the in-plane bending moment, I_y is the area moment of inertia w.r.t. y-axis, and V is the shear force.

The nominal stress is, then, obtained by calculating the Von Mises stress σ_{VM} from the normal and shear stress.

$$\sigma_{VM} = \sqrt{\sigma_N^2 + 3\tau_{xy}^2} \tag{4.19}$$

The axial force, bending moment and shear force at the mudline are evaluated from the PDEs, which are expressed as (Metrikine (2005))

$$M_y(z,t) = E\,I_y \frac{\partial^2 u_n}{\partial z^2}, \quad V(z,t) = E\,I_y \frac{\partial^3 u_n}{\partial z^3} + T(z)\frac{\partial u_n}{\partial z}, \quad N_z(z,t) = T(z) \tag{4.20}$$

in which the continuous partial derivatives are discretized in terms of spatial displacement in Appendix A.

Also, along the tubular member, the structural detailing, such as the eccentricity between the welded plates, leads to the increase in local stresses in comparison to the nominal stresses. Such stresses are termed as *Hot Spot Stress (HSS)* and are derived by multiplying the nominal stresses by the stress concentration factor SCF.

$$\sigma_{HSS} = SCF \cdot \sigma_{VM} \tag{4.21}$$

In the current study, the SCF of 1.5 was applied in accordance with Det Norske Veritas (2012).

4.4.2. RAINFLOW COUNTING METHOD

Fatigue damage is usually obtained by counting the number of occurrence of stress ranges in a period; generally performed using the cycle counting methods. The rainflow counting method is the most widely accepted method for fatigue assessment; first proposed by Matsuishi and Endo (1968). The detailed description of this counting method can be found in Stephens et al. (2001) and is not repeated here. To summarize, the stress time history (Equation 4.21) is subjected to rainflow counting algorithm that divides the stress amplitudes into stress ranges and counts the number of cycles occurring per amplitude range. The advantage of this method is that it also includes small amplitude peaks, which makes fatigue damage calculation more accurate.

4.4.3. PALMGREN-MINER RULE

Fatigue design of welded structures is usually based on the constant amplitude tests. However, due to the presence of random or stochastic stress amplitude, the evaluation of fatigue damage is generally referred to as cumulative fatigue damage (Marin, 2014). Numerous cumulative damage theories can be found in the literature to asses the fatigue damage. The linear damage model, originally proposed by Palmgren (1924) and later developed by Miner (1945), commonly referred to as *Palmgren-Miner (or Miner's) rule* is most widely used cumulative damage model for the failures caused by fatigue.

Miner's rule is the simplest model that calculates the damage increment for each stress levels and sums up all the damage increment to obtain the cumulative fatigue damage.

$$D = \sum_{i=1}^{n} \frac{n_i}{N_i} \tag{4.22}$$

where n_i is the number of cycles accumulated at stress level S_i obtained from rainflow counting method, N_i is the number of cycles to failure at the i^{th} stress level S_i based on the S-N curve, n is the number of stress cycle, and D is the cumulative fatigue damage on the basis of particular S-N curve.

'S-N curve' mentioned earlier, also known as Wøhler curve, is a graphical representation of the magnitude of an alternating stress range versus the number of cycles, that indicates how many cycles N at certain stress S the material can endure before failure. The relationship between the number of cycles to failure N and the stress range is given by Det Norske Veritas (2012). The design S-N curve used in this study was the 'C1 curve in seawater'.

5

RESULTS AND DISCUSSIONS

This chapter presents the results generated by the FD model described in the Chapter 4. First, in Section 5.1, the dynamic ice-structure interaction is studied as a function of ice sheet velocity in the absence of aerodynamics. Additionally, the structural response at the ice action point and the tower top are discussed in detail during the three interaction regimes of ice-induced vibrations. Finally, in Section 5.2, the effect of rotor aerodynamics on the ice-structure interaction are presented. To demonstrate its impact on the ice-induced vibrations, the results are compared with the ice-only case. Reiterating, the fatigue damage as a function of ice sheet velocity is discussed at the end of each section to quantify the effect of control idling on the ice-induced vibrations.

5.1. IDENTIFICATION OF ICE-INDUCED VIBRATIONS

To investigate the dynamic ice-structure interaction upon level ice interacting with the offshore structure, the model is first subjected to the ice action only. The interaction regimes of ice-induced vibrations were studied by varying the ice-sheet velocity. For each ice-drift speed, the simulations were performed for 300s, in which the first 150s were disregarded to reduce the transient effect of the initial conditions.

5.1.1. FREQUENCY LOCK-IN RELATION

To distinguish the three regimes of ice-induced vibrations over the range of ice-drift velocities, the frequency lock-in relation described in Sec. 2.1.2 was used as guidance. A graph of maximum structural velocity versus ice drift speed is depicted in Figure 5.1 for a damped structure (Rayleigh damping) subjected to the level ice action.

From the Figure 5.1, the clear distinction can be made between the three regimes of ice-induced vibrations predicted by the FD model.

1. For ice velocities from **5mm/s to 60mm/s**, the maximum relative velocity between the ice and structure is considerably high, which is usually observed during intermittent crushing due to the failure of ice elements. As soon as the ice failure is triggered, there is a significant reduction in the contact area between the ice

and structure, and as a result, the structure starts moving towards the ice, thereby causing the increase in the relative velocity.

2. One of the key features of frequency lock-in is the linear relationship between the maximum structural velocity and ice sheet velocity. The slope of the linear relationship β lies between the 1.0 and 1.5, as explained in Sec. 2.1.2. For the range of ice velocities from **60mm/s to 210mm/s**, it can be deduced that ice-structure interaction lies within the frequency lock-in regime. Realistically, the upper bound velocity of 210mm/s is significantly high for an offshore wind turbine to experience the frequency lock-in. This occurrence in the result could be due to the choices taken while modelling the ice-structure interaction.

3. Lastly, for the ice velocities higher than **210mm/s**, the continuous brittle crushing regime can be seen.

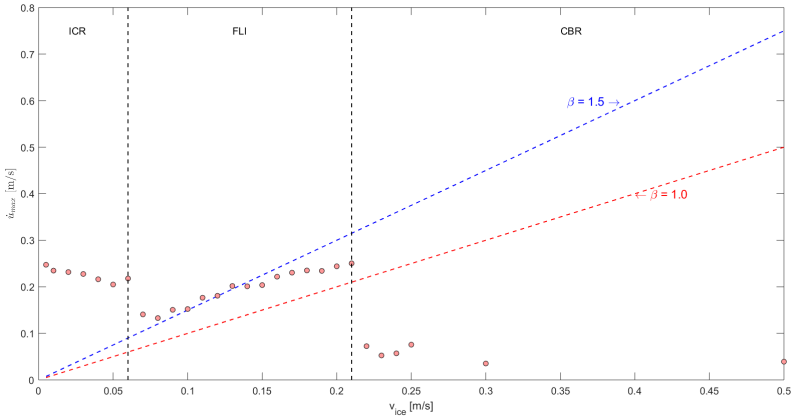

Figure 5.1: Obtained maximum velocity of structure at ice action point as a function of ice sheet velocity. Abbreviations: ICR - Intermittent crushing, FLI - Frequency lock-in, CBR - Continuous brittle crushing, Vertical dashed lines denotes the range of ICR, FLI and CBR.

5.1.2. GLOBAL LOAD AND MAXIMUM DISPLACEMENT

The ice-induced vibration regimes are further confirmed by the general trends of the statistical measure of global ice load and displacements in the FD model, depicted in Figure 5.2. Statistical values are determined from the second half of the total time signal, as explained earlier.

The general trend of global ice load is first presented by Hendrikse (2017) based on the simulations performed on the flexible structure. He demonstrated that the mean and maximum global ice loads are largest in the intermittent crushing regime and reduces to a more or less constant value for high indentation velocities. The transition to frequency lock-in and continuous brittle crushing lie around the velocities when the mean and maximum global load levels off, without the clear identification of individual regimes over the range of velocities. A similar trend of reducing maximum and mean global ice load can be observed in the Figure 5.2.

Marsman (2018), on the other hand, explained these regimes based on the statistical measure of maximum displacement over the range of ice velocities for a jacket-type support structure. At low ice-drift speed, the build-up of global ice load results in the higher amplitudes of structural displacement. Around the first transition velocity of ICR and FLI, there is a sudden drop in the displacement followed by the gradual increase in amplitude with the increasing ice velocities. The CBR starts at the second transition velocity, where the amplitude of structural displacement is considerably small compared to the other two regimes. The similar trend can be seen in the current wind support structure too (Figure 5.2).

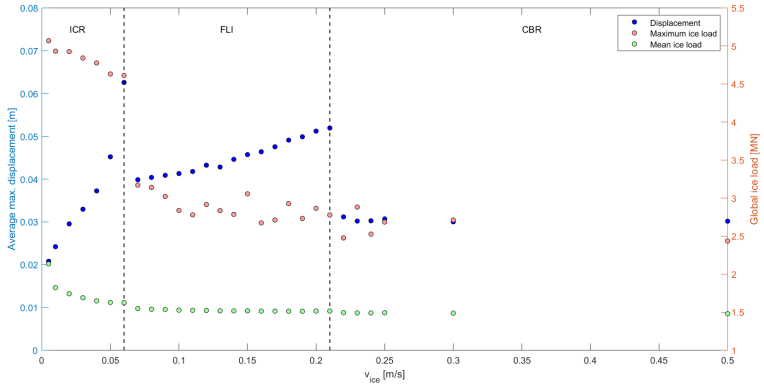

Figure 5.2: Average maximum structural displacement at ice action point, maximum global ice load and mean global ice load as a function of ice sheet velocity.

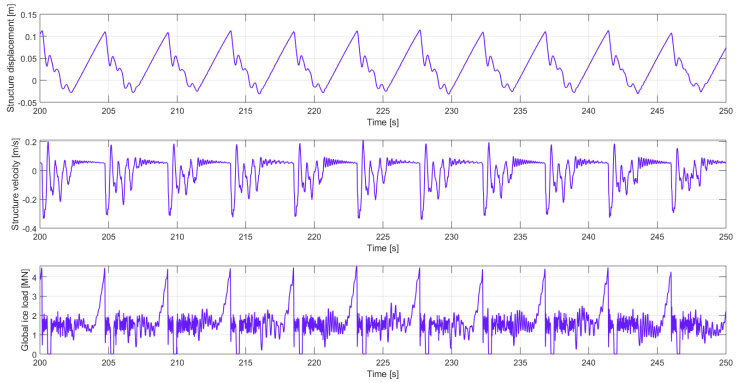

Figure 5.3: From top to bottom: time traces of structural displacement, structural velocity, and ice load at the ice-action point in ICR regime for an ice velocity of 60mm/s.

5.1.3. STRUCTURAL RESPONSE AT ICE ACTION POINT

To gain a better insight of ice-structure interaction, the time traces of structural displacement, structural velocity and global ice load at ice-action point are depicted in Fig-

ures 5.3, 5.4, and 5.5. A qualitative observation of a time signal in Figure 5.3 at an ice velocity of 60mm/s suggests the occurrence of intermittent crushing; saw tooth pattern of displacement and global ice load.

In Figure 5.4, harmonic oscillations around the second natural frequency of the structure can be clearly observed in displacement and velocity signal at an ice velocity of 210mm/s. Additionally, the ice load is correlated to the structural velocity; increase in the load during the period when relative velocity is low, and synchronized to the natural frequency of the structure. These characteristics suggest the occurrence of frequency lock-in regime.

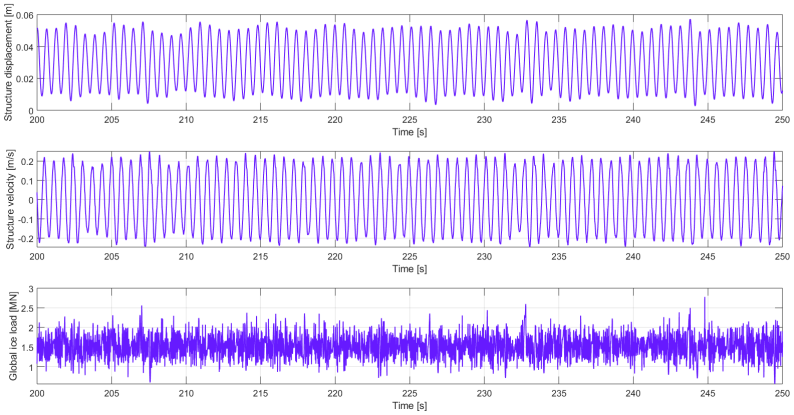

Figure 5.4: From top to bottom: time traces for structural displacement, structural velocity, and ice load at the ice-action point in FLI regime for an ice velocity of 210mm/s.

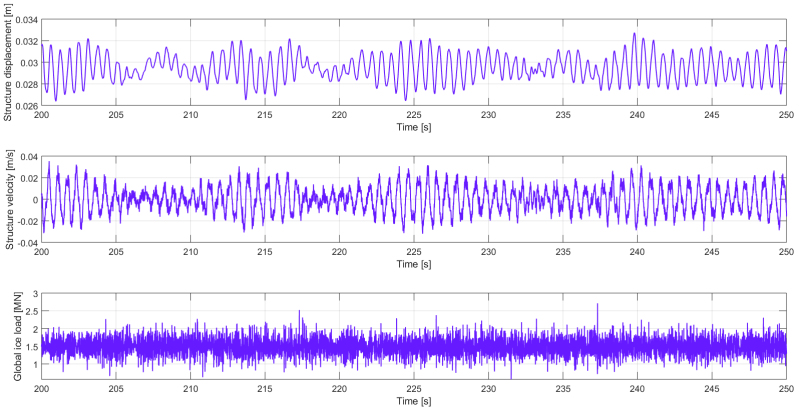

Figure 5.5: From top to bottom: time traces for structural displacement, structural velocity, and ice load at the ice-action point in CBR regime for an ice velocity of 300mm/s.

Lastly, in Figure 5.5, continuous brittle crushing can be seen at an ice velocity of

300mm/s. The structural response is characterized by the small amplitude oscillations around the equilibrium; significantly smaller in comparison to intermittent crushing and frequency lock-in. Also, the obtained ice load has no apparent periodicity and the signal is random in nature.

Next, in Figure 5.6, the contour plot of structural response frequency spectrum at the ice-action point as a function of ice-drift speed is illustrated. For low ice velocities, in the intermittent crushing regime, the majority of energy is contained around the frequency of the saw-tooth pattern, which lies below the first natural frequency of the structure.

In the frequency lock-in regime, the frequency increases towards the second natural frequency, but stays slightly below it; consistent with the similar observations presented in Hendrikse (2017). Furthermore, the reasoning behind the second mode of vibration is attributed to the modal amplitude at the ice action point (Table 4.4); the second mode has a higher value as compared to the first mode of vibration.

The maximum difference in the response frequency is observed during the start of frequency lock-in, which gradually reduces with increasing ice sheet velocity. The reason for the reduction is the resistance of ice before the brittle fracture, that delays the structure from moving back towards its equilibrium position; presented by Hendrikse and Metrikine (2015) based on the results obtained from its numerical model.

At higher velocities in the continuous brittle crushing regime, the structure undergoes small oscillations around the second natural frequency of the structure; except at certain velocities, for example at an ice sheet velocity of 230mm/s, where it has the coupling in the first and second bending mode of the structure.

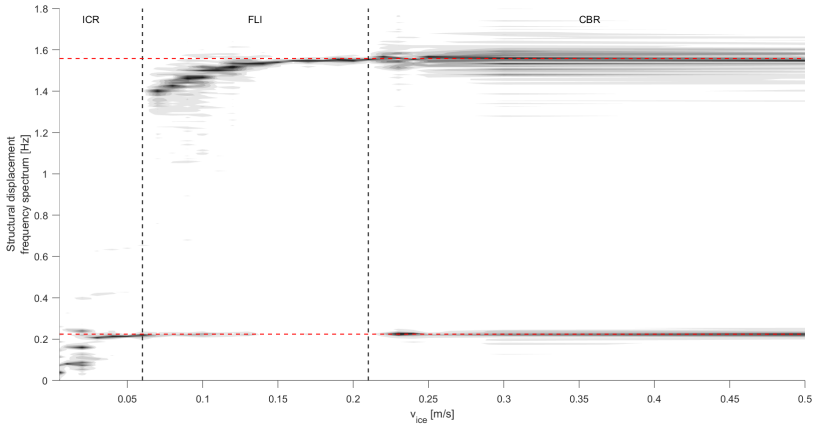

Figure 5.6: Contour map of structural response frequency spectrum plotted against the ice sheet velocity. Black contours indicate the maximum energy content of the spectrum. The horizontal red dashed lines represents the first two natural frequencies of the structure.

5.1.4. STRUCTURAL RESPONSE AT TOWER TOP

The global ice load acting at the MSL has the energy content over the range of natural frequencies of the structure. It can excite certain fundamental modes that can cause significant vibrations at the tower top, thereby considerably impacting the RNA. Figure 5.7

shows the trend of average maximum displacement as a function of ice sheet velocity at the tower top. The trend observed in the intermittent crushing regime is similar to the trend at ice action point depicted in Figure 5.2. However, the displacement in the frequency lock-in and the continuous brittle crushing regime are almost same; unlike the increasing displacement trend seen at the ice action point during frequency lock-in.

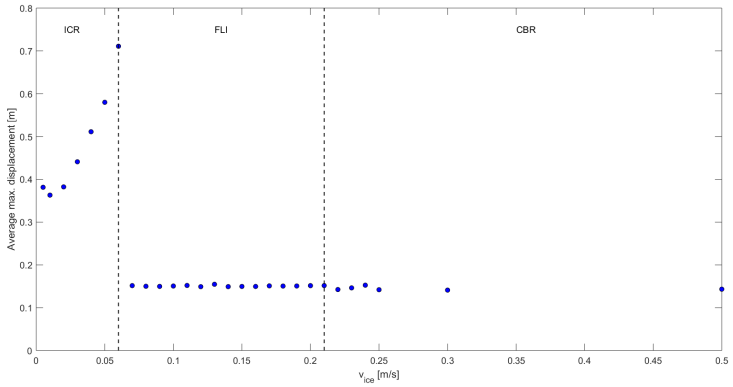

Figure 5.7: Average maximum structural displacement at the tower top as a function of ice sheet velocity.

The conceivable explanation for the observed behaviour is given through the displacement time signal depicted in Figure 5.8. In intermittent crushing regime, the frequency of excitation is close to the first natural frequency of the structure. Additionally, the modal amplitude of the first mode is significantly higher than the other structural modes of vibration (Table 4.4). Thus, the structural response at the tower top can extract energy relatively easy from the ice and undergoes sustained vibration in its first mode.

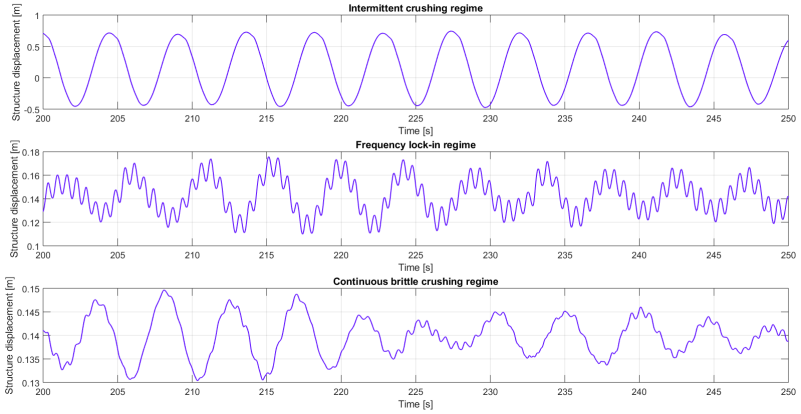

Figure 5.8: Structural displacement at tower top as a function of time. Top: intermittent crushing at an ice velocity of 60mm/s. Middle: Frequency lock-in regime at an ice velocity of 210mm/s. Bottom: Continuous brittle crushing at an ice velocity of 320mm/s.

During the frequency lock-in and continuous brittle crushing, the frequency content of the ice energy is present primarily around the second natural frequency of the structure. Due to the modal damping and low modal amplitude in the second mode (Table 4.4), the resulting vibrations at the tower top is associated with small oscillations around the second natural frequency of the structure.

5.1.5. FATIGUE DAMAGE DUE TO THE ICE LOAD ONLY

Generally, in order to calculate the fatigue damage accurately, it is typical to obtain 1-hour stochastic realization, according to Det Norske Veritas (2013). Additionally, the fatigue damage needs to be evaluated based on the probability of occurrence of different ice conditions. Both of these requirements were neglected in this study as the former is computationally expensive, and the latter falls outside the scope of this study. Thus, the aim is not to predict fatigue damage accurately, but rather enable the reader to understand the general trend of fatigue damage as a function of ice velocity. The simplest and perhaps the extremely conservative approach is to assume that the damage from the 150s simulation always occur for all the ice conditions. The 1-year damage presented in the Figure 5.9 is extrapolated from 150s simulation according to Equation 5.1.

$$D_{year} = D \cdot \frac{3600}{150} \cdot 24 \cdot 365 \tag{5.1}$$

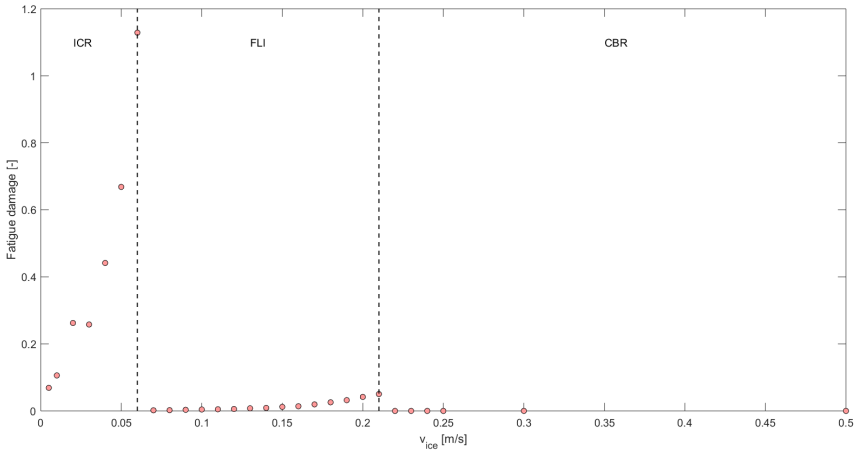

Figure 5.9: Fatigue damage at mudline as a function of ice velocity.

From the Figure 5.9, the maximum damage is predicted in the intermittent crushing regime at an ice velocity of 60mm/s. Since the hot spot stresses at the mudline were calculated from the nodal displacements (Sec. 4.4), the fatigue damage follows the increasing trend similar to the maximum displacement, as shown in the Figure 5.2.

From the Figure 5.9, it can also be deduced that the most significant damage occurs when the loading is applied in the first mode of vibration (Figure 5.6). Also, the fatigue damage during frequency lock-in is significantly small in comparison to the intermittent

crushing. This can be explained by looking at the Figure 5.2 again. It shows a relatively smaller amplitude of vibrations (or maximum displacement) in the second mode, implying the lower bending moment at the mudline and thus, lesser damage. In continuous brittle crushing regime, as expected, the fatigue damage is significantly small in comparison to the other two regimes.

5.2. CONTROL IDLING

In this section, the results of simulations from the combined wind and ice case are compared with the ice-only case to gain insight into the aerodynamic effect on the ice-structure interaction. The control idling of wind turbine was performed by subjecting the ice-structure model to rotor aerodynamics below the cut-in wind speed. To this end, the range of rotational rotor speeds employed were 3.0rpm, 6.9rpm, and 12.1rpm. We opted for these rotor speeds as it helps in understanding the different flow states of the wind turbine rotor. Hereafter, the results presented in all the subsections are for these rotational speeds only.

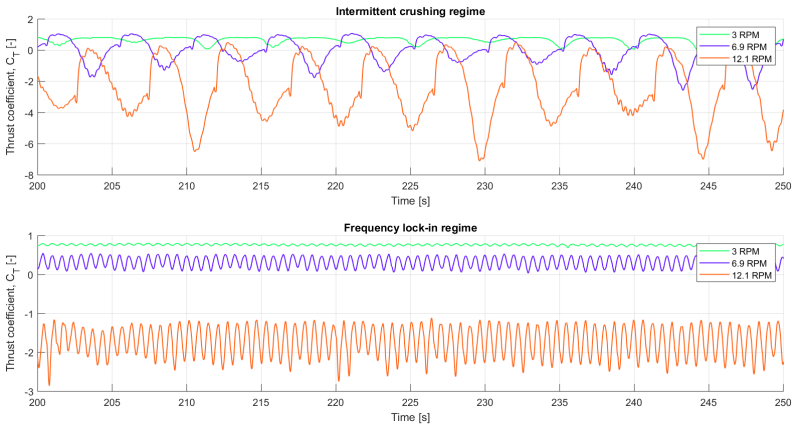

Figure 5.10: Thrust coefficient time signal over the range of rotational rotor speed during intermittent crushing (ICR) and frequency lock-in (FLI). Ice sheet velocity pertaining to ICR and FLI is 40mm/s and 180mm/s, respectively.

5.2.1. EFFECT OF AERODYNAMIC LOADING

Prior to the discussion on the effect of rotor aerodynamics on ice-structure interaction, an understanding of unsteady aerodynamics and the aerodynamic damping ratio are presented in this section. The focus of this section is to gain a thorough understanding of the unsteady BEM method in the ice-structure interaction process.

Explained earlier in Sec. 3.2, the rotor can enter four different flow states due to the presence of unsteady aerodynamics. These flow states are identified from the time traces of thrust coefficient and inflow velocity ratio presented in the Figures 5.10 and 5.11, respectively.

The behaviour of rotor aerodynamics in the ice-induced vibration regimes, observed from the thrust coefficient time signal, Figure 5.10, are as follows:

1. ***Intermittent crushing regime***: In this regime, the tower top undergoes excessive vibrations in the first bending mode that lead to a rapid change of effective wind speed seen by the turbine blades. These rapid changes in the relative velocity cause the rotor to cycle between the windmill state and the propeller state; identified by the positive and negative thrust coefficient upon comparing with the Figure 3.3. Findings for the different rotor speeds are:

   (a) *Rotor speed of 3.0rpm*: Interestingly, the rotor remains in a windmill state (positive thrust coefficient) for all the ice-sheet velocities, except for the ice-drift speed of 60mm/s, when the thrust coefficient is found to vary between the positive and negative value;

   (b) *Rotor speed of 6.9rpm*: The cycling between the two states occurs for all the ice-sheet velocities;

   (c) *Rotor speed of 12.1rpm*: Rotor primarily behaves as a propeller (negative thrust coefficient) for all the ice-sheet velocities, except on a few time instants, when the thrust coefficient changes to a small positive value;

   (d) Magnitude of thrust coefficient increases with increasing rotor speeds. This can be explained by the relative wind velocity seen by the turbine blades. In the propeller state, the turbine moves in the direction of the wind, and therefore, has higher relative velocity as compared to the windmill state. This results in a larger angle of attack (Eq. 3.7), and thus, a larger thrust force.

2. ***Frequency lock-in regime***: The tower top motions are relatively less severe due to the vibrations in the second bending mode. In this regime, the change of rotor flow states is mainly governed by the tip speed ratio. At higher tip speed ratio, the rotor starts interacting with its own wake; thus transitioning from windmill to vortex ring state and approaches towards the propeller state. Findings for the different rotor speeds are:

   (a) *Rotor speed of 3.0rpm and 6.9rpm*: Rotor mainly operates in the windmill state;

   (b) *Rotor speed of 12.1rpm*: Higher tip speed ratio implies that the rotor starts behaving as a propeller, shedding energy into the flow field;

   (c) Magnitude of the thrust coefficient at 3rpm rotor speed is larger than it is at 6rpm. The most straightforward explanation is that with the similar relative velocity at the turbine blades and smaller rotational speed, the angle of attack is larger, and therefore, the rotor thrust force is larger for the rotor speed of 3rpm.

Similar observation is further explained through the Figure 5.11, which is adapted from Leble and Barakos (2016), where V_c is the inflow velocity normal to the rotor plane (negative sign is introduced to agree with the notations used for helicopter), and v_h is the induced velocity in "helicopter hover" for the given thrust force T and the rotor area A. Both the parameters are expressed as

$$V_c = -\left(U_\infty - \dot{u}\right), \quad v_h = \sqrt{\frac{T}{2\rho A}} \tag{5.2}$$

Along with distinguishing the different flow states, Figure 5.11 demonstrates the clear identification of time instants when the BEM theory breaks down. As explained by Sebastian and Lackner (2013), because of the severe drop in effective wind speed, the rotor starts interacting with its own wake, leading to the development of recirculation areas normal to the rotor disc. This phenomenon is referred to as "Vortex ring state", where the BEM theory completely breaks down and cannot accurately predict the aerodynamic loads.

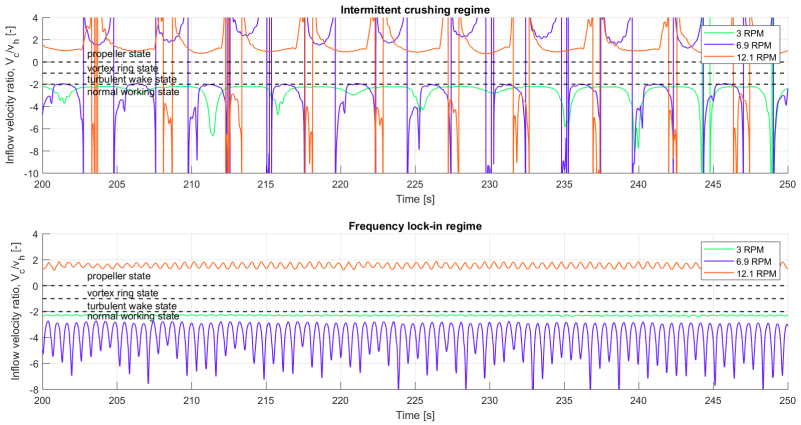

Figure 5.11: Inflow velocity ratio time signal over the range of rotational rotor speed during intermittent crushing (ICR) and frequency lock-in (FLI). Ice sheet velocity pertaining to ICR and FLI is 40mm/s and 180mm/s, respectively.

The large overshoot of inflow ratio in the Figure 5.11 is the result of the positive and negative fluctuation of induced velocity v_h with the thrust force T. This overshoot is believed to be associated with the vortex ring state, which the current unsteady BEM model cannot predict, and therefore, instantaneously jumps to either the propeller state or the windmill state. It must be emphasized here that with a more advanced aerodynamic model such as the "Simplified Free Vortex Wake method", the vortex ring state can be easily captured. However, this is beyond the scope of the current study.

For convenience reason, the behaviour of rotor aerodynamics is presented similarly as the thrust coefficient. The observed behaviours are as follows:

1. ***Intermittent crushing regime***: Findings for the different rotor speeds are:

   (a) *Rotor speed of 3.0rpm*: No breakdown occurs, except for an ice-sheet velocity of 60mm/s;

   (b) *Rotor speed of 6.9rpm*: The breakdown (or the overshoot) occurs more frequently;

   (c) *Rotor speed of 12.1rpm*: The breakdown in the rotor aerodynamics is found on a few time instants when the rotor suddenly transits from the propeller to windmill state.

2. ***Frequency lock-in regime***: Findings for the different rotor speeds are:

   (a) *Rotor speed of 3.0rpm and 12.1rpm*: No breakdown found, indicating the unsteady BEM theory model can predict the rotor aerodynamics accurately;

   (b) *Rotor speed of 6.9rpm*: No breakdown observed in the Figure 5.11. However, it does occur on a few time instants for the specific ice-drift speeds.

This transition between different flow states, especially in the intermittent crushing regime, is commonly seen in the floating offshore wind turbines undergoing pitching motion, rendering the flow field highly complex and unsteady. This has been extensively studied by Sebastian and Lackner (2013), Leble and Barakos (2016), and Lienard et al. (2019).

From these results, it can be concluded that the unsteady BEM model has certain limitations, especially in the intermittent crushing regime. For instance, the loads predicted by the aerodynamic model cannot be relied upon for the rotor speed of 6.9rpm. Furthermore, during the intermittent crushing, due attention must be exercised on drawing a general conclusion for the rotational speeds of 3.0rpm and 12.1rpm. Interestingly, in the frequency lock-in regime, the current aerodynamic model has the ability to accurately capture the rotor aerodynamics, except for the rotor speed of 6.9rpm, where the momentum theory breaks down on few time instants at the specific ice-drift speeds.

AERODYNAMIC DAMPING RATIO

The aerodynamic damping in the structure is determined by the method proposed by Salzmann and Tempel (2005). His method is quite straightforward and gives the reader a quick insight into the damping introduced in the structural model. The aerodynamic damping c_{AD}, according to this method, is determined as the increase in the thrust force dT per unit increase in the wind speed dU; instantaneous wind speed calculated at the rotor hub. Moreover, the aerodynamic damping ratio ξ_{AD} as a percentage of critical damping is determined as given in Equation 5.3.

$$c_{AD} = \frac{dT}{dU}, \quad \xi_{AD} = \frac{c_{AD}}{2\,M_n\,\omega_n} \tag{5.3}$$

where M_n is n$^{\text{th}}$ modal mass, and ω_n is the n$^{\text{th}}$ natural frequency of the tower.

The identified damping ratio as a percentage of critical damping in the first bending mode is depicted in Figure 5.12. The damping ratios in higher modes were not studied in detail since the majority of ice-induced response occurs in the first and second bending modes only.

As one would have expected, the aerodynamic damping during intermittent crushing regime fluctuates between the positive and negative values. Positive damping during windmill state and negative damping during the propeller state, indicating that in latter the energy is being imparted to the flow. Similar inference can be made during frequency lock-in too. However, unlike intermittent crushing, it does not excessively fluctuate between the positive and negative values; explained earlier in Sec. 5.2.1. Furthermore, the magnitude of damping is relatively higher during the intermittent crushing due to the higher amplitude tower top motion in the first bending mode, which leads to the higher

thrust force. Additionally, in the frequency lock-in regime, the damping is higher at 3rpm as compared to 6rpm rotational rotor speed due to the relatively larger thrust force.

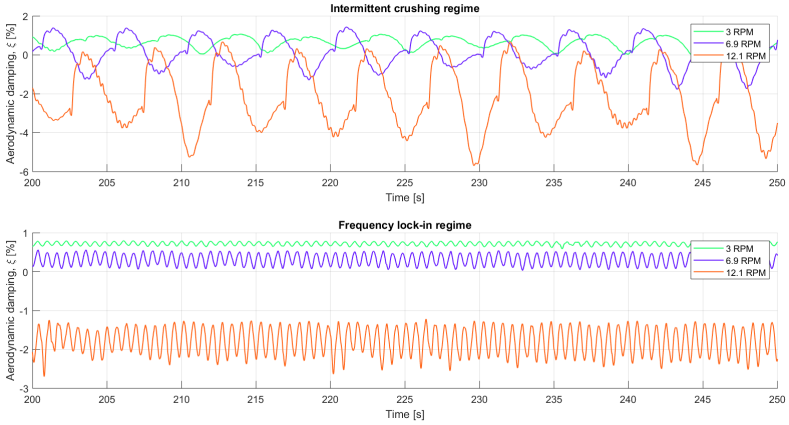

Figure 5.12: Aerodynamic damping, as a percentage of critical, over range of rotational rotor speeds during ICR and FLI. Ice sheet velocity pertaining to ICR and FLI is 40mm/s and 180mm/s, respectively.

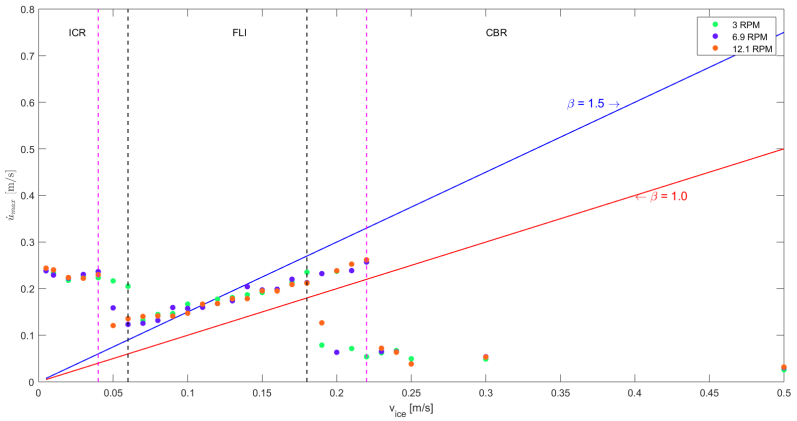

Figure 5.13: Obtained maximum velocity of structure at ice action point as a function of ice sheet velocity. Vertical black dashed lines denotes the range of ICR, FLI and CBR. Vertical black and pink dashed lines denotes the range of ICR, FLI and CBR for rotor speeds of 3.0rpm, and 6.9rpm & 12.1rpm respectively.

5.2.2. FREQUENCY LOCK-IN RELATION

Similar to Sec. 5.1.1, three regimes of ice-induced vibrations over a range of ice velocities, and rotational rotor speed were distinguished through frequency lock-in relation. From the Figure 5.13, the following observations were made for the structure subjected to combined wind and ice action.

1. The range of frequency lock-in for the rotor speeds of 6.9rpm and 12.1rpm is

50mm/s to 220mm/s. The lower bound range of ice sheet velocities has reduced in the presence of aerodynamics. However, there has been no impact on the upper bound velocity, which is because of the relatively low aerodynamic damping. Hendrikse (2017) has found through numerical studies that higher damping reduces the range of velocities over which frequency lock-in develops, where the effect is more pronounced for the upper velocity than the lower velocity. This effect can be clearly seen for the rotor speed of 3.0rpm, where the range is reduced to **70mm/s to 180mm/s**.

2. Intermittent crushing range is shifted to **5mm/s to 40mm/s** for rotor speeds of 6.9rpm and 12.1rpm as compared to the range 5mm/s to 60mm/s with "no aerodynamics" case. However, for the rotational rotor speed of 3rpm, the range of ice sheet velocity remains similar to the range with the ice-only case.

3. Lastly, the range of velocity over which continuous brittle crushing occurs is from **230mm/s** onwards for the rotor speeds of 6.9rpm and 12.1rpm, and from **190mm/s** onwards for the rotor speed of 3.0rpm.

5.2.3. GLOBAL LOAD AND STRUCTURAL RESPONSE AT ICE ACTION POINT

The effect of aerodynamic loading to the ice-structure interaction at the ice action point during intermittent crushing and frequency lock-in is analyzed in this section. During the continuous brittle crushing, the interaction between the ice and structure is insignificant and therefore, is not important for the design of the offshore wind support structures.

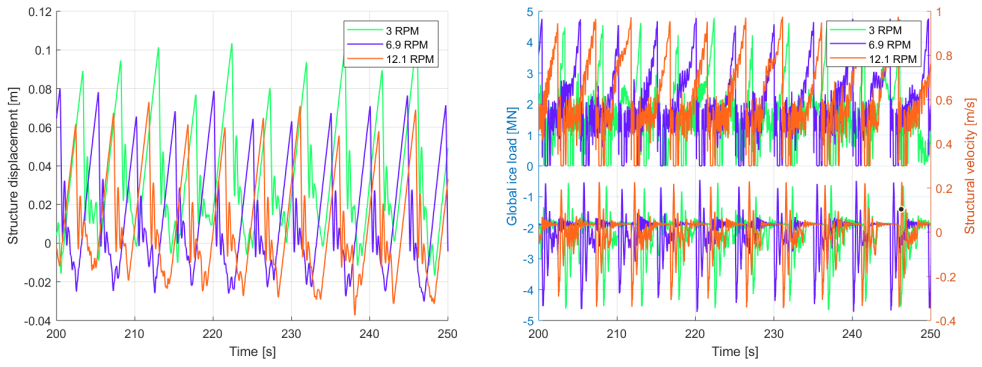

(a) Structural displacement

(b) Top: Global ice load. Bottom: Structural velocity

Figure 5.14: Structural displacement, velocity and global ice load time signal at the ice action point over the range of rotational rotor speeds during the ICR. Ice sheet velocity pertaining to ICR is 40mm/s.

Figure 5.14 depicts the time traces of structural displacement, structural velocity and ice load in the intermittent crushing regime at an ice-sheet velocity of 40mm/s. From the Figure 5.14a, the amplitudes of structural displacement are 48mm, 45mm and 44mm for the rotor speeds of 3.0rpm, 6.9rpm and 12.1rpm, respectively. Upon comparing with the

ice-only case, the response amplitude is found to be 47mm for the same ice-sheet velocity. This indicates that the control idling has some impact in damping the vibrations, except for the rotor speed of 3.0rpm. The reason behind this is two-fold; firstly, the presence of higher aerodynamic damping for the rotor speeds of 6.9rpm and 12.1rpm, and secondly, the structural response frequency being close to the first natural frequency, implying that the force acting at the tower top can influence the structural vibrations at the ice action point (see Sec. 4.2.3 for detailed explanation). Also, the rotor aerodynamics has an impact on the mean displacement too; 45mm, 20mm and 18mm for the rotor speeds of 3.0rpm, 6.9rpm and 12.1rpm, respectively, and 40mm in the absence of aerodynamic loading. This is mainly due to the presence of thrust force at the tower top; higher and negative thrust force at 12.1rpm further reducing the mean value.

The global ice load in the presence and the absence of rotor aerodynamics remains approximately the same, as depicted in the Figure 5.14b. The ice-structure interaction is greatly influenced by the relative velocity between the structure and the ice at the ice action point. And, by looking closely at the structural velocity during the load build-up phase in the Figures 5.3 and 5.14b, it is almost similar, which in turn explains why the maximum global ice load remains approximately the same.

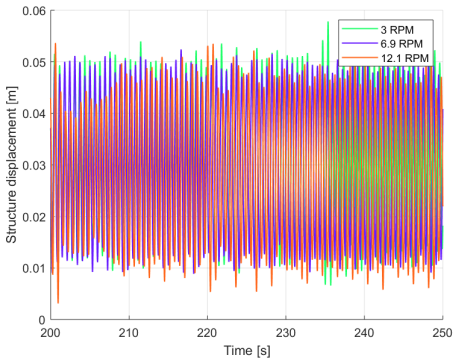

(a) Structural displacement

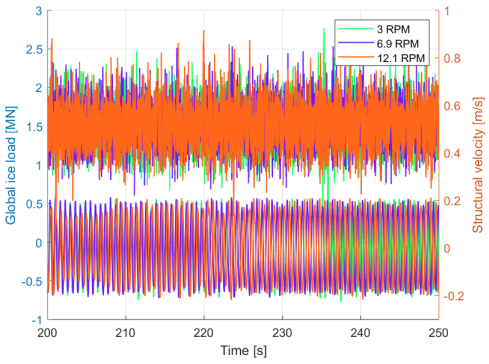

(b) Top: Global ice load. Bottom: Structural velocity

Figure 5.15: Structural displacement, velocity and global ice load time signal at the ice action point over the range of rotational rotor speeds during the FLI. Ice sheet velocity pertaining to FLI is 180mm/s.

Likewise, the time traces during the frequency lock-in at an ice velocity of 180mm/s are depicted in the Figure 5.15. Drawing a similar comparison, it can be seen that the displacement amplitude (Figure 5.15a) remains almost similar both in the presence and the absence of aerodynamics. The conceivable reasoning behind this is the location of the thrust force that has a higher modal amplitude at the tower top in the first mode. Thus, it has a higher impact in damping the vibrations in the first bending mode rather than the second mode; second natural frequency being the response frequency during the FLI. Also, the relatively small aerodynamic damping is offset by the relatively large modal amplitude at the ice action point in the second mode. For the mean displacement, the explanation similar to intermittent crushing hold. In the end, for the global ice load, once again the structural velocity is comparable in the absence and the pres-

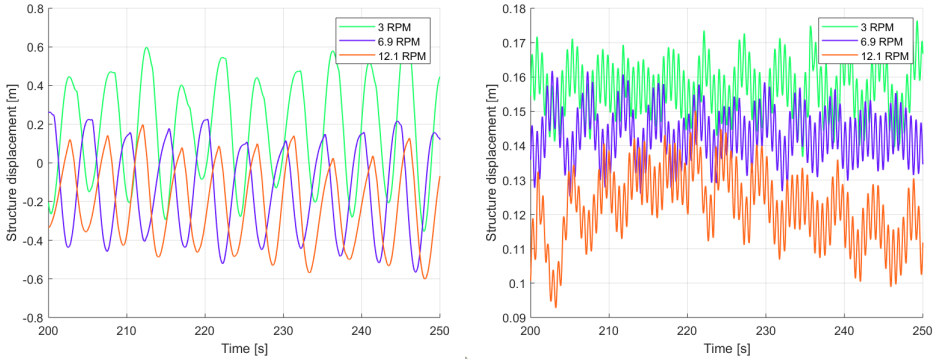

(a) Structural displacement in ICR

(b) Structural displacement in FLI

Figure 5.16: Structural displacement time signal at the tower top over the range of rotational rotor speeds during the ICR and the FLI. Ice sheet velocity pertaining to ICR and FLI is 40mm/s and 180mm/s, respectively.

ence of aerodynamics (Figures 5.15b and 5.4), resulting into the similar global ice load.

5.2.4. STRUCTURAL RESPONSE AT TOWER TOP

Figure 5.16 depicts the structural response at tower top during intermittent crushing and frequency lock-in at rotor speeds of 3.0rpm, 6.9rpm and 12.1rpm. Explained earlier in Sec. 5.1.4 and to reiterate, during intermittent crushing, the tower top oscillates harmonically in the first natural frequency, whereas in the frequency lock-in, the oscillations are primarily around the second natural frequency.

During intermittent crushing, the amplitude of oscillations in the absence of aerodynamics is around 350mm for an ice-sheet velocity of 40mm/s. At 6.9rpm rotational rotor speed, this amplitude is 300mm, and at 12.1rpm, the amplitude of oscillations is 270mm. Thus, the influence of aerodynamic damping can be clearly seen in damping the tower top vibrations. However, the amplitude is not significantly reduced by increasing the rotor rotational speed, primarily due to the change of flow state from the windmill to the propeller and thereby, not considerably affecting the magnitude of aerodynamic damping. On the other hand, at a rotor speed of 3.0rpm, the amplitude of vibrations is 340mm, which is significantly high in comparison to the rotor speeds of 6.9rpm and 12.1rpm. The simple reason is the relatively low aerodynamic damping depicted in Figure 5.12.

In frequency lock-in regime, the structure oscillates in second natural frequency on the top of the first bending mode. The amplitude of oscillations under the ice-action case is approximately 11mm for an ice-sheet velocity of 180mm/s. In the presence of aerodynamic, the amplitude reduces to around 8mm at rotor speeds of 3.0rpm, 6.9rpm and 12.1rpm. The relatively small damping of vibrations is attributed to low aerodynamic damping during the frequency lock-in (refer to Sec. 5.2.1).

5.2.5. FATIGUE DAMAGE DUE TO ICE AND WIND

Lastly, the influence of rotor aerodynamic on fatigue damage is illustrated in Figure 5.17. Additionally, in the same figure, the comparison is drawn with respect to the fatigue

damage in the absence of rotor aerodynamics. Findings for different rotor speeds in the intermittent crushing regime are discussed below.

1. *Rotor speed of 3.0rpm*: There is an increase in the fatigue damage as compared to the case with "no aerodynamics". This is mainly because of the relatively low aerodynamic damping in combination with the additional bending moment at the mudline due to the thrust force;

2. *Rotor speed of 6.9rpm*: There is a significant reduction in fatigue damage for an ice sheet velocity of 40mm/s. This agrees with the explanation provided for the structural response in the previous sections;

3. *Rotor speed of 12.1rpm*: There is an increase in the fatigue damage as compared to the case with "no aerodynamics", except for an ice sheet velocity of 40mm/s. A simple explanation is: the low aerodynamic damping is offset by the additional bending moment at the mudline. The observation at an ice-drift speed of 40mm/s agrees well with the explanation provided for the structural response in the previous sections.

At this point, it is important to let the reader know that the fatigue damages for ice sheet velocities below 40mm/s for the rotor speed of 6.9rpm are not accurate enough to draw any conclusion. This is mainly due to the breakdown of unsteady BEM model, resulting into the incorrect thrust forces and structural response at the tower top.

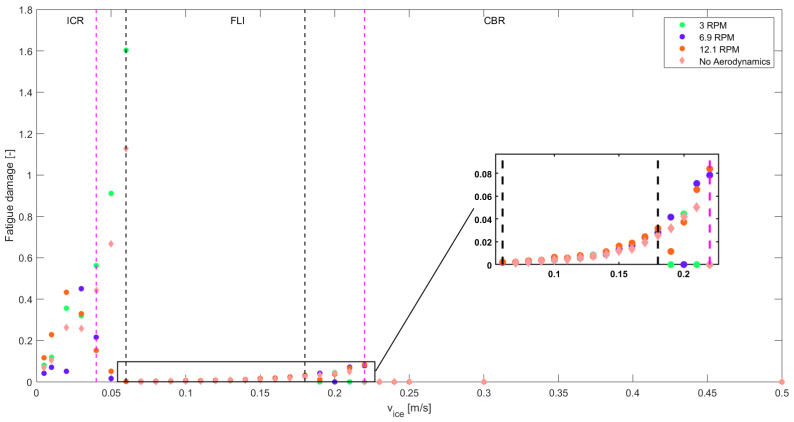

Figure 5.17: Fatigue damage at mudline as a function of ice velocity in the presence and the absence of rotor aerodynamics.

There is a significant reduction in fatigue damage during the frequency lock-in in comparison to the "no aerodynamics" case for the ice-sheet velocities of 50mm/s and 60mm/s for rotational rotor speeds of 6.9rpm and 12.1rpm. The simple explanation is; during the absence of aerodynamics these ice drift speeds falls into the intermittent crushing regime, which in the presence of aerodynamics has moved into frequency lock-in regime. This shift in regime impacts the structural response frequency, from the first to second natural frequency, and significantly influences the fatigue damage.

Moreover, by looking at the magnified image for the ice sheet velocities from 70mm/s to 220mm/s, surprisingly there is an increase in fatigue damage in the presence of aerodynamics. The possible reason can be found by looking at the aerodynamic damping during the frequency lock-in. The inability of rotor aerodynamics in damping the vibrations substantially, combined with the additional bending moment at the mudline due to the thrust force at the tower top, results in higher fatigue damage during the frequency lock-in.

6

CONCLUSIONS AND RECOMMENDATIONS

The main goal of this thesis was to investigate numerically that the ice-induced vibrations in offshore wind turbines can be mitigated by the control idling method. The work was divided into three separate sub-objectives to achieve the main goal. The fulfilment of these research objectives, along with the conclusions, is discussed in Sec. 6.1. Ultimately, in Sec 6.2, recommendations are offered to further improve and expand on the research performed in this study.

6.1. CONCLUSIONS

The first research objective was to create a model for non-linear dynamic ice-structure interaction of offshore wind turbine; this was accomplished in Chapter 4. To this end, first, the literature study into ice action on the flexible, vertically sided offshore structures was performed in Chapter 2. Based on the studies, it was shown that the ice-induced vibrations can develop in such structures, and three regimes are generally distinguished, viz. intermittent crushing, frequency lock-in, and continuous brittle crushing. Among these regimes, the intermittent crushing and frequency lock-in are of particular interest; they can cause significant vibrations in offshore structure. At the end of the Chapter 2, the phenomenological ice model developed by Hendrikse et al. (2019) was presented along with the ice model input parameters adopted in the study.

In Chapter 4, the UpWind reference wind turbine model was implemented based on the *Finite Difference* method. To reduce the computational time, the higher structural modes were disregarded by employing a reduced-order modal analysis technique, since their contribution is not important in the overall response of the structure. The susceptibility of eigenmodes to the force acting at the ice-action point is investigated by performing eigenanalysis and frequency response function analysis. It was found that first and second modes can extract energy relatively easily and therefore, can undergo sustained vibrations upon ice-structure interactions.

The second research objective was to create an aerodynamic model that can capture rotor aerodynamics of a rotor rotating below the cut-in wind speed. Blade-element-

momentum (BEM) method is the most common method in wind engineering applications. Literature study on BEM in Chapter 3 resulted in some important observations. The traditional BEM method is based on the steady flow conditions and thus does not accurately capture the rotor aerodynamics in the unsteady environment. Furthermore, due to the unsteadiness, the rotor can enter four different flow states depending upon the tip speed ratio. In the current study, it was found that the rotor can transit from windmill state to propeller state at higher rotational speeds, thereby resulting in positive to negative thrust force at the tower top. Unsteady aerodynamics are generally distinguished into two types, viz. unsteady profile aerodynamics and dynamic inflow. The time scale of the latter is of the order that is comparable to the natural period of the structure and is therefore chosen in the current study. This unsteadiness is implemented into the steady BEM method using the "Stig Øye Dynamic Inflow" engineering model. Finally, the coupling between the ice-structure interaction and the rotor aerodynamics is performed in Chapter 4.

Lastly, the third objective was to investigate the effectiveness of rotor aerodynamics in mitigating the vibrations. First, in Section 5.1, a study was performed where the offshore wind turbine model is subjected to the ice-only action. It was found that the ice-structure model can accurately predict the three regimes of ice-induced vibrations for varying ice-sheet velocities. Furthermore, it was observed that the frequency of the structural response is close to the first natural frequency during the intermittent crushing, and the second natural frequency during the frequency lock-in regime. For the same reason, the structural response at the tower top is associated with relatively high amplitude of vibrations during intermittent crushing. At the end of the section, the fatigue damage at the mudline is presented. It was observed that the damage in intermittent crushing regime is significantly higher as compared to the frequency lock-in regime.

Afterwards, in Section 5.2, the results from the combined wind and ice case were compared with the ice-only case by employing the following rotational speeds: 3.0rpm, 6.9rpm and 12.1rpm. Applicability of the unsteady BEM model during intermittent crushing and frequency lock-in was illustrated for these rotational rotor speeds. It was found that the unsteady BEM model has certain limitations, especially in the intermittent crushing regime, because of the breakdown of the momentum theory during the vortex-ring flow state. In the frequency lock-in regime, the aerodynamic model has the ability to accurately capture the rotor aerodynamics, except for the rotor speed of 6.9rpm, where the momentum theory breaks down on few time instants. Interestingly, during the intermittent crushing, the rotor flow state cycles between the windmill and the propeller state; usually found when floating offshore wind turbine undergoes pitching motion. But, during the frequency lock-in, it either remains in the windmill state (for 3.0rpm & 6.9rpm) or in the propeller state (for 12.1rpm).

Next, the aerodynamic damping was determined in a simplistic manner based on the instantaneous thrust force. The damping, in general, was found to be higher during intermittent crushing as compared to the frequency lock-in. However, no notable impact was observed on the range of ice-induced vibration regimes for the rotor speed of 6.9rpm and 12.1rpm because of the presence of low aerodynamic damping. For the rotor speed of 3.0rpm, there is an apparent reduction in the range of frequency lock-in, and thereby, showing the effectiveness of rotor aerodynamics on the ice-induced vibrations. A fa-

tigue damage comparison was then made between the coupled model and the model with the ice-only case. During the intermittent crushing, no conclusion can be drawn on the damage for the rotor speed of 6.9rpm due to inaccurate structure response at the tower top; except at an ice sheet velocity of 40mm/s, where a reduction in the damage was observed. On the other hand, for the rotor speeds of 3.0rpm and 12.1rpm, in general, there is an increase in the fatigue damage in the intermittent crushing regime. Also, in the frequency lock-in regime, the similar increase in fatigue damage was observed. For both, this increase is the result of the combined effect of low aerodynamic damping and the additional bending moment at the mudline.

Based on the results, it is concluded that the rotor aerodynamics does help in damping the vibrations in the intermittent crushing regime by increasing the rotor rotational speed. On the other hand, in the frequency lock-in regime, it has no significant impact. It can also be confirmed that by the careful selection of the rotational rotor speed, the range of ice-induced vibration regimes can be influenced. However, to draw the general conclusion, the analysis needs to be conducted for varied ranges of rotor speeds. Also, the present framework of the aerodynamic model needs to be improved to capture the vortex-ring flow state in order to predict the rotor aerodynamics accurately for all the ice-sheet velocities.

6.2. RECOMMENDATIONS

Several recommendations for further research can be proposed considering the current study as a basis for mitigating the ice-induced vibrations in offshore wind turbine structure. Pertaining to the rotor aerodynamics, the current unsteady BEM model could be improved to capture the vortex-ring flow state. One of the possible ways is to implement "Simplified Free Vortex Wake" aerodynamic model instead of unsteady aerodynamics. Free wake analysis is better suited for complex aerodynamic flow states occurring during the intermittent crushing, and therefore, provides a more realistic representation of rotor aerodynamics of offshore wind turbine. Furthermore, the pattern control idling can be investigated by actively or passively changing the blade pitch angle in such a manner that it influences the relative velocity between the ice and the structure at the ice-action point. This might help in mitigating the vibrations during the intermittent crushing regime. Lastly, the study could be extended to the normal operating condition of the wind turbine using the unsteady aerodynamic model. This will introduce higher aerodynamic damping and might have a considerable impact on the ice-induced vibration regimes.

Another set of recommendations are regarding the modelling of the offshore wind turbine. The ice-induced vibrations have energy content over the range of frequencies. Some of these frequencies could excite the flapwise mode of the rotor blade, thus incorporating blade dynamics could provide more insight into the aero-ice-structure interaction. Moreover, the ice-structure interaction during the normal operating condition can cause lateral tower vibration in the side-side direction. This in combination with low aerodynamic damping of the rotor in side-side direction, could shorten the fatigue life of the structure. Thus, extending the research to side-side lateral vibrations could result in a much better understanding of the dynamic ice-structure interaction of offshore wind turbine.

REFERENCES

Athanasia Arapogianni, Anne-Bénédicte Genachte, and Ochagavia. Deep water - The next step for offshore wind energy. *European Wind Energy Association*, Jul. 2013.

Anne Barker, Garry Timco, Helge Gravesen, and Per Vølund. Ice loading on Danish wind turbines: Part 1: Dynamic model tests. *Cold Regions Science and Technology*, 41(1): 1–23, Jan. 2005.

Ilmas Bayati, Marco Belloli, and Alberto Zasso. A Formulation For The Unsteady Aerodynamics Of Floating Wind Turbines, With Focus On The Global System Dynamics. *In: Proceedings of the International Conference on Offshore Mechanics and Arctic Engineering - OMAE*, OMAE2017-61925, 2017.

A. Betz. Das Maximum der theoretisch möglichen Ausnützung des Windes durch Windmotoren. *Zeitschrift für das gesamte Turbinenwesen*, 26:307–309, 1920. (In German).

Bo Bjork. *Ice-induced vibration of fixed offshore structures. part 2: Experience with Baltic lighthouses.* Ship Research Institute of Norway, Information Department, 1981.

Thomas G. Brown and Mauri Määttänen. Comparison of Kemi-I and Confederation Bridge cone ice load measurement results. *Cold Regions Science and Technology*, 55 (1):3–13, Jan. 2009.

Tony Burton, Nick Jenkins, David Sharpe, and Ervin Bossanyi. *Wind Energy Handbook.* John Wiley & Sons, Incorporated, 2 edition, Jun. 2011.

Det Norske Veritas. DNV-RP-C203 Fatigue Design of Offshore Steel Structures. Oct. 2012.

Det Norske Veritas. DNV-OS-J101 Design of Offshore Wind Turbine Structures. Jan. 2013.

S. Drzewiecki. Bulletin L'Association Technique Maritime. 1892.

Bengt Fornberg. Generation of finite difference formulas on arbitrarily spaced grids. *Mathematics of Computation*, 51(184):699–706, 1988.

R. Frederking and J. Schwarz. Model test of ice forces on fixed and oscillating cones. *Cold Regions Science and Technology*, 6:61–72, 1982.

R.E. Froude. On the part played in propulsion by differences of fluid pressure. *Transaction of the Institute of Naval Architects*, 30:390–405, 1889.

W. Froude. On the Elementary Relation between Pitch, Slip, and Propulsive Efficiency. *Transaction of the Institute of Naval Architects*, 19:47, 1878.

H. Glauert. *Airplane propellers.* Springer, Berlin, Heidelberg, 1935. Divison L.

Helge Gravesen and Tuomo Kärnä. Ice Loads for offshore wind turbines in southern baltic sea. *Proceedings of the 20th International Conference on Port and Ocean Engineering under Arctic Conditions*, 2009.

Helge Gravesen, Søren L. Sørensen, Per Vølund, Anne Barker, and Garry Timco. Ice loading on Danish wind turbines: Part 2: Analyses of dynamic model test results. *Cold Regions Science and Technology*, 41(1):25–47, Jan. 2005.

Martin O. L. Hansen. *Aerodynamics of Wind Turbines (3rd Edition)*. Routledge, 2015.

H. Hendrikse. *Ice-induced vibrations of vertically sided offshore structures*. PhD thesis, Delft University of Technology, 2017.

Hayo Hendrikse and Andrei Metrikine. Interpretation and prediction of ice induced vibrations based on contact area variation. *International Journal of Solids and Structures*, 75-76:336–348, Sept. 2015.

Hayo Hendrikse, T. S. Nord, and Andrei Metrikine. A model for determining the dynamic response of offshore structures interacting with a crushing ice floe. *Wind Energy*, 2019.

P. C. J. Hoogenboom and R. Spaan. Shear Stiffness and Maximum Shear Stress of Tubular Members. *International Offshore and Polar Engineering Conference*, June 2005.

IEC-61400. Design requirements for offshore wind turbines. IEC document 88/642/CDV (Committee draft for vote of second edition of IEC 61400-3, now renumbered as IEC 61400-3-1). July 2017.

ISO 19906. Petroleum and natural gas industries - Arctic offshore structures. *International Standard*, 2010.

M.G. Jefferies and W.H. Wright. Dynamic response of Molikpaq to ice-structure interaction. *Proceedings of the 7th International Conference on Offshore Mechanics and Arctic Engineering*, 4, 1988.

J. Jonkman, S. Butterfield, W. Musial, and G. Scott. Definition of a 5-MW Reference Wind Turbine for Offshore System Development. *National Renewable Energy Laboratory*, Feb. 2009.

Tuomo Kärnä. Mitigation of steady-state vibrations induced by ice. *Proceedings of the International Offshore and Polar Engineering Conference*, April 1994.

Tuomo Kärnä and Kari Kolari. Mitigation of dynamic ice actions on offshore wind turbines. *Proceedings of the third European Conference on Structural Control*, July 2004.

V Leble and G Barakos. Forced pitch motion of wind turbines. *Journal of Physics: Conference Series*, 753(2):1101–1114, Sept. 2016.

J.G. Leishman. *Principles of Helicopter Aerodynamics*, volume 12 of *Cambridge Aerospace Series*. Cambridge University Press, 2 edition, 2016.

Matti Leppäranta. An ice drift model for the Baltic Sea. *Tellus*, 33(6):583–596, 1981.

Haoran Li, Zhiqiang Hu, Jin Wang, and Xiangyin Meng. Short-term fatigue analysis for tower base of a spar-type wind turbine under stochastic wind-wave loads. *International Journal of Naval Architecture and Ocean Engineering*, 10:9–20, 2018.

Caroline Lienard, Ronan Boisard, and Camille Daudin. Aerodynamic behavior of a floating offshore wind turbine. *AIAA Scitech*, Jan. 2019.

E Lourens, C Papadimitriou, S Gillijns, E Reynders, G De Roeck, and G Lombaert. Joint input-response estimation for structural systems based on reduced-order models and vibration data from a limited number of sensors. *Mechanical Systems and Signal Processing*, 2012.

Traian I. Marin. Fatigue Analysis of Column-Pontoon Connection in a Semi-submersible Floating Wind Turbine. *Delft University of Technology, and Norwegian University of Science and Technology*, 2014.

Irene Marsman. Ice-induced vibrations of wind turbines with a jacket support structure. *Master thesis, Delft University of Technology*, Dec. 2018.

M. Matsuishi and T. Endo. Fatigue of metals subjected to varying stress. *Japan Society of Mechanics Engineering, Fukuoka, Japan*, pages 37–40, 1968.

A. V. Metrikine. Dynamics, Slender Structures and an Introduction to Continuum Mechanics. *Faculty of Civil Engineering and Geosciences, Delft University of Technology*, 2005.

M. A. Miner. Cumulative Damage in Fatigue. *Journal of Applied Mechanics*, 67(3):159–164, 1945.

Arkadiusz Mróz, Jan Holnicki-Szulc, and Tuomo Kärnä. Mitigation of ice loading on offshore wind turbines: Feasibility study of a semi-active solution. *Computers & Structures*, 86:217–226, 2008.

Biadgo Mulugeta and Aynekulu Gerawork. Aerodynamic Design of Horizontal Axis Wind Turbine Blades. *FME Transaction*, 45:647–660, Jan. 2017.

A. Palmgren. Durability of Ball Bearings. *Zeitschrift des Vereines Deutscher Ingenieure (ZVDI)*, 68(14):339–341, 1924. in German.

W.J.M. Rankine. On the Mechanical Principles of the Action of Propellers. *Transaction of the Institute of Naval Architects*, 6:13–39, 1865.

H. Salani and H. Matlock. A FINITE-ELEMENT METHOD FOR TRANSVERSE VIBRATIONS OF BEAMS AND PLATES. *Development of Methods for Computer Simulation of Beam-Columns and Grid-Beam and Slab Systems*, 56(8):201–213, 1967.

D.J.C. Salzmann and J. van der Tempel. Aerodynamic damping in the design of support structures for offshore wind turbines. *In: European offshore wind conference*, 2005.

T Sebastian and Matthew A. Lackner. Characterization of the unsteady aerodynamics of offshore floating wind turbines. *Wind Energy*, 16:339–352, 2013.

Marc Seidel and Hayo Hendrikse. Analytical assessment of sea ice-induced frequency lock-in for offshore wind turbine monopiles. *Marine Structures*, 60:87–100, Apr. 2018.

K. Shkhinek, S. Kapustiansky, and A. Jilenkov. Ice loads onto the sloping structures. *International Conference on Development and Commercial Utilization of Technologies in Polar Regions*, pages 171–178, 1996.

H. Snel and J. G. Schepers. Engineering moles for dynamic inflow phenomena. *Journal of Wind Engineering and Industrial Aerodynamics*, 39:267–281, May 1992.

H. Snel and J. G. Schepers. Joint investigation of dynamic inflow effects and implementation of an engineering method. *Technical Report ECN-C-94-107*, 1995.

J.M.J Spijkers, A.W.C.M. Vrouwenvelder, and E.C. Klaver. Structural Dynamics CT 4140. *Faculty of Civil Engineering and Geosciences, Delft University of Technology*, Jan. 2005.

J. N. Sørensen, W. Z. Shen, and X. Munduate. Analysis of Wake States by a Full-field Actuator Disc Model. *Wind Energy*, 1(2):73–88, 1998.

Ralph I. Stephens, Ali Fatemi, Robert R. Stephens, and Henry O. Fuchs. *Metal Fatigue in Engineering (2nd Edition)*. John Wiley & Sons, 2001.

J.B. de Vaal, M.O.L. Hansen, and T. Moan. Effect of wind turbine surge motion on rotor thrust and induced velocity. *Wind Energy*, 17(1):105–121, May 2014.

V. Valamanesh and A. T. Myers. Aerodynamic Damping and Seismic Response of Horizontal Axis Wind Turbine Towers. *Journal of Structural Engineering*, 140(11), Nov. 2014.

W E Van Der Deijl. Dynamic wind speed in Dynamic Inflow models. *Master thesis, Delft University of Technology*, July 2018.

W. de Vries. Final report WP 4.2: Support Structure Concepts for Deep Water Sites: Deliverable D4.2.8 (WP4: offshore foundations and support structures). *UpWind project WP 4.2*, 2011.

Shengyong Wang, Qianjin Yue, and Dayong Zhang. Ice-induced non-structure vibration reduction of jacket platforms with isolation cone system. *Ocean Engineering*, 70:118–123, July 2013.

E. Wessels and K. Kato. Ice forces on fixed and floating conical structures. *Proceedings 9th International IAHR Symposium on Ice*, pages 666–691, 1988.

R. E. Wilson, P. B. S. Lissaman, and S. N. Walker. Aerodynamic Performance of Wind Turbines. *ERDA/NSF/04014-7611*, 1976.

Q J Yue and L Li. Ice Problems in Bohai Sea Oil Exploitation. *Proceedings of the 17th International Conference on Port and Ocean Engineering under Arctic Conditions*, 2003.

Qianjin Yue and Xiangjun Bi. Ice-Induced Jacket Structure Vibrations in Bohai Sea. *Journal of Cold Regions Engineering*, 14(2):81–92, 2000.

Qianjin Yue, Li Zhang, Wenshou Zhang, and Tuomo Kärnä. Mitigating ice-induced jacket platform vibrations utilizing a TMD system. *Cold Regions Science and Technology*, 56 (2-3):84–89, May 2009.

Li Zhang, Qianjin Yue, Wenshou Zhang, and C Hsiao. Experimental study on mitigation of ice-induced vibration for offshore platforms with a tuned mass damper. *Proceedings of the Institution of Mechanical Engineers Part M Journal of Engineering for the Maritime Environment*, 222(3):121–132, Mar. 2008.

A

MODELLING OF OFFSHORE WIND TURBINE

This appendix describes in detail the formulation of a multi-degree-of-freedom structural model that is presented in Chapter 4. First, in Section A.1, the governing equations of motion describing the lateral fore-aft bending vibration is defined along with the boundary condition. Next, in Section A.2, the Finite Difference Method (FDM) numerical method is explained, i.e. the formulation of spatial derivatives in terms of the spatial coordinates. Finally, in Section A.3, the modal analysis solution technique is described.

A.1. EQUATION OF MOTIONS

A schematic representation of a typical offshore wind turbine undergoing vibration in lateral fore-aft direction is depicted in Figure A.1. The tower and support structure were discretized into "N" finite Euler-Bernoulli beam elements having "$N+1$" nodes. Each node was associated with one transversal DOF, viz. the fore-aft motion. RNA was modelled as a rigid structure implying the blade bending vibrations were not taken into account in the current study.

The governing equations of motion describing the fore-aft bending vibrations of the structural model are given by the following Partial Differential Equations (PDE).

$$EI_1 \frac{\partial^4 u_1}{\partial z^4} + \frac{\partial}{\partial z}\left(T_1(z)\frac{\partial u_1}{\partial z}\right) + \rho A_1 \frac{\partial^2 u_1}{\partial t^2} + K_1 u_1 = 0, \qquad -h \le z \le -d \tag{A.1a}$$

$$EI_2 \frac{\partial^4 u_2}{\partial z^4} + \frac{\partial}{\partial z}\left(T_2(z)\frac{\partial u_2}{\partial z}\right) + (\rho A_2 + \mu_2)\frac{\partial^2 u_2}{\partial t^2} = 0, \qquad -d \le z \le 0 \tag{A.1b}$$

$$EI_3 \frac{\partial^4 u_3}{\partial z^4} + \frac{\partial}{\partial z}\left(T_3(z)\frac{\partial u_3}{\partial z}\right) + \rho A_3 \frac{\partial^2 u_3}{\partial t^2} = 0, \qquad 0 \le z \le L \tag{A.1c}$$

where $i = 1,2,3$ representing the different parts of the structure, u_i is the displacement in positive x-direction representing the DOF of the continuous beam, EI_i is the bending stiffness, ρ is the mass density of steel, A_i is the cross-sectional area of tubular members,

A

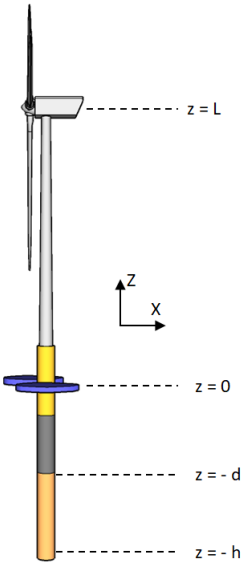

Figure A.1: Schematic representation of an offshore wind turbine in level ice conditions undergoing vibrations in fore-aft direction.

K_1 is the constant linear soil stiffness, and μ_2 is the added mass of the underwater part of the structure.

$T_i(z)$ in Equation A.1b is the axial compressive force along the length of the structure that accounts for the loss of stiffness due to the compression softening, given by

$$T_i(z) = M_{top}\, g + \rho A_i\, g\, (L - z) \tag{A.2}$$

where M_{top} is the total mass of RNA, g is the gravitational constant, and z is the vertical coordinates along the length of the structure.

The pinned boundary conditions at $z = 0$, representing the bottom of the structure embedded into the soil, are given by the following equation:

$$u_1(-h, t) = \left.\frac{\partial^2 u_1}{\partial z^2}\right|_{z=-h} = 0 \tag{A.3}$$

The top of the tower is rigidly connected to the RNA, which is subjected to the unsteady aerodynamic loading described in Chapter 3. The resulting thrust force ($F_{thrust}(t)$) is implemented into the boundary conditions at the tower top, which are expressed as:

$$\left.\frac{\partial^2 u_3}{\partial z^2}\right|_{z=L} = 0 \tag{A.4a}$$

$$EI_3 \left.\frac{\partial^3 u_3}{\partial z^3}\right|_{z=L} = F_{thrust}(t) + M_{top} \left.\frac{\partial^2 u_3}{\partial t^2}\right|_{z=L} \tag{A.4b}$$

Lastly, the coupling between ice and structure is introduced by employing interface conditions at MSL. These conditions ensure that the displacement, slope, bending moment, and shear force are continuous between the different parts of the structure. The ice action, therefore, is taken into account as the abrupt change in the shear force interface condition at MSL, given by:

$$\left(EI_3\frac{\partial^3 u_3}{\partial z^3}+T_3(z)\frac{\partial u_3}{\partial z}-EI_2\frac{\partial^3 u_2}{\partial z^3}-T_2(z)\frac{\partial u_2}{\partial z}\right)\Bigg|_{z=0}=F_{ice}(u_2,t)\Bigg|_{z=0} \tag{A.5}$$

A.2. FINITE DIFFERENCE METHOD

Finite Difference Method (FDM) spatially discretize the PDE into a set of an ordinary differential equation (ODE), which then can be solved numerically using an ODE solver. The formulation of spatial derivative in terms of spatial coordinates with second order accuracy $\mathcal{O}(l^2)$ is derived by Fornberg (1988). The spatial derivatives that are relevant for the current study are reproduced in Equation A.6.

$$\frac{\partial u_n}{\partial z}\approx\frac{1}{l}\left(-\frac{1}{2}u_{n-1}+\frac{1}{2}u_{n+1}\right)+\mathcal{O}(l^2) \tag{A.6a}$$

$$\frac{\partial^2 u_n}{\partial z^2}\approx\frac{1}{l^2}\left(u_{n-1}+2\,u_n+u_{n+1}\right)+\mathcal{O}(l^2) \tag{A.6b}$$

$$\frac{\partial^3 u_n}{\partial z^3}\approx\frac{1}{l^3}\left(-\frac{1}{2}u_{n-2}+u_{n-1}-u_{n+1}+\frac{1}{2}u_{n+2}\right)+\mathcal{O}(l^2) \tag{A.6c}$$

$$\frac{\partial^4 u_n}{\partial z^4}\approx\frac{1}{l^4}\left(u_{n-2}-4\,u_{n-1}+6\,u_n-4\,u_{n+1}+u_{n+2}\right)+\mathcal{O}(l^2) \tag{A.6d}$$

where l represents the element length, and u_n is the displacement of the beam at node n.

By substituting the spatial derivatives in terms of nodal displacements into the governing equation of motions (Equation A.1), along with the boundary and interface conditions, the PDE in time and space domain is translated into the time domain ODE. Assembling the coefficients of nodal accelerations and displacements yield the following system of "N" equations of motion:

$$\mathbf{M}\ddot{\mathbf{u}}(t)+\mathbf{C}\dot{\mathbf{u}}(t)+\mathbf{K}\mathbf{u}(t)=\mathbf{f}(t) \tag{A.7}$$

where the structure's mass, stiffness, and damping matrices are denoted by $(\mathbf{M},\mathbf{K},\mathbf{C})\in\mathbb{R}^{N\times N}$ respectively, and the force vector is represented by $\mathbf{f}(t)\in\mathbb{R}^N$.

A.3. MODAL ANALYSIS

In the modal analysis, eigenmodes $\mathbf{\Phi}$ form a complete basis to describe the dynamic behaviour of the system. The structural displacement $\mathbf{u}(z,t)$ is, therefore, written as the linear combination of the products between the $\mathbf{\Phi}$, accounting for spatial variations, and $\boldsymbol{\eta}(t)$, accounting for time dependence, as follows:

$$\mathbf{u}(z,t)=\mathbf{\Phi}\,\boldsymbol{\eta}(t) \tag{A.8}$$

where $\mathbf{\Phi}$ was determined in Equation 4.7 and $\boldsymbol{\eta}(t) \in \mathbb{R}^N$ is the modal displacement vector.

Substituting Equation A.8 into the Equation A.7 and pre-multiplying by the transpose of the eigenvectors $\mathbf{\Phi}^T$, yields the following:

$$\underbrace{\mathbf{\Phi}^T \mathbf{M} \mathbf{\Phi}}_{\mathbf{M}^*} \ddot{\mathbf{u}} + \underbrace{\mathbf{\Phi}^T \mathbf{C} \mathbf{\Phi}}_{\mathbf{C}^*} \dot{\mathbf{u}} + \underbrace{\mathbf{\Phi}^T \mathbf{K} \mathbf{\Phi}}_{\mathbf{K}^*} \mathbf{u} = \underbrace{\mathbf{\Phi}^T \mathbf{f}}_{\mathbf{f}^*} \tag{A.9}$$

Due to the orthogonality of eigenvectors with respect to the mass and stiffness, the resulting modal mass ($\mathbf{M}^*$) and stiffness ($\mathbf{K}^*$) matrices are diagonal. Furthermore, since the damping matrix $\mathbf{C}$, determined in Sec. 4.2.2, is the linear combination of mass and stiffness matrix, the resulting modal damping matrix $\mathbf{C}^*$ is diagonal as well. Thus, the coupled system of equations (Equation A.7) simplifies to the decoupled set of differential equations, given by:

$$\mathbf{M}^* \ddot{\boldsymbol{\eta}}(t) + \mathbf{C}^* \dot{\boldsymbol{\eta}}(t) + \mathbf{K}^* \boldsymbol{\eta}(t) = \mathbf{f}^* \tag{A.10}$$

where the modal mass, damping and stiffness matrices are written as

$$\mathbf{M}^* = \begin{bmatrix} 1 & & & \\ & 1 & & \\ & & \ddots & \\ & & & 1 \end{bmatrix} \tag{A.11}$$

$$\mathbf{C}^* = \begin{bmatrix} 2\xi_1\omega_1 & & & \\ & 2\xi_2\omega_2 & & \\ & & \ddots & \\ & & & 2\xi_N\omega_N \end{bmatrix} \tag{A.12}$$

$$\mathbf{K}^* = \begin{bmatrix} {\omega_1}^2 & & & \\ & {\omega_2}^2 & & \\ & & \ddots & \\ & & & {\omega_N}^2 \end{bmatrix} \tag{A.13}$$

where ξ_i is the modal damping ratio and ω_i is the natural frequency of the system.